Journal of Ceramic Processing Research. Vol. 25, No. 5, pp. 875~903 (2024)
(Received 15 July 2024, Received in revised form 21 July 2024, Accepted 11 September 2024)
https://doi.org/10.36410/jcpr.2024.25.5.875

J O U R N A L O F
Ceramic Processing Research

Present status and prospects of thermal barrier coating materials: A review

Jiahang Liu[a], Yiyong Wang[a], Zhe Lu[a,*], Yeon-Gil Jung[b,*], Guanlin Lyu[c], Yanwen Zhou[a], Jing Zhang[d] and Yan Li[a]
[a]*School of Materials and Metallurgical Engineering, University of Science and Technology Liaoning, Anshan 114051, China*
[b]*School of Materials Science and Engineering, Changwon National University Changwon, Gyeongnam 51140, Korea*
[c]*Key Lab of New Ceramics and Fine Processing, School of Materials Science and Engineering, Tsinghua University, Beijing 10084, China*
[d]*Department of Mechanical Engineering, Indiana University-Purdue University Indianapolis, Indianapolis, IN 46202-5132, USA*

Thermal barrier coatings (TBCs) are a surface technology applied to the hot parts of turbine engines by depositing on the surface of nickel-based high-temperature alloys to reduce the surface temperature of the substrate. However, the continual pursuit of higher service temperatures can lead to degradation, delamination, and premature failure of surface coatings. To meet the future service requirements of advanced thermal barrier coating systems, it is necessary to develop new ceramic materials. This work summarized the research progress of advanced thermal barrier coatings ceramic materials in recent years, including ZrO_2-based ceramic materials, $A_2B_2O_7$-type ceramic materials, rare-earth phosphates, rare-earth hafnates, yttrium aluminum garnet, perovskite oxides, magnetoplumbite compounds, high-entropy ceramics, rare-earth tantalates, rare-earth niobates, and rare-earth silicates. The structures and properties of various materials were summarized, and the advantages and shortcomings were described. Finally, the development directions of advanced thermal barrier coating materials were envisioned to guide the development of new thermal barrier coatings.

Keywords: Thermal barrier coating, Ceramic material, Thermophysical properties, Doping modification, Review.

Introduction

Aero-engines and land-based gas turbines are highly complex and sophisticated thermal machines that play a vital role in industrial development [1]. Turbine gas temperature is a significant indicator of advanced gas turbine technology [2]. Along with the gradual increase in performance, the turbine components' thermal loads and temperature gradients have increased dramatically. At present, the temperature of the turbine inlet of an engine with a thrust-to-weight ratio of 10:1 reaches 1800-2000 K; the temperature of the turbine inlet of an engine with a thrust-to-weight ratio of 15-20:1 reaches 2100-2300 K, which is much higher than the melting point of high-temperature alloy materials for the hot-end components of the engine [3, 4]. Based on the development trend of the engine, the development of higher-grade high-temperature materials, the design of efficient blade cooling structures, the preparation of advanced single-crystal high-temperature alloy blades, and the development of advanced thermal barrier coatings (TBCs) are essential solutions [5, 6]. Among them, the thermal barrier coatings technology can effectively improve the thrust-to-weight ratio and thermal efficiency of aero-engines, gas turbines, rocket engines, and supersonic vehicles [7].

Thermal barrier coatings are complex multilayer structural coatings. Conventional thermal barrier coating systems usually consist of four parts: a nickel-based high-temperature alloy; a metal-bond coat (BC); a ceramic top coat (TC); and a thermally grown oxide layer (TGO) that forms in a high-temperature environment [8, 9]. With the development of coating preparation technology, single ceramic coat structure, multi-layer ceramic coat structure, and gradient ceramic coat structure coatings have emerged [10]. Each part of the coating has a unique role. The bond coat acts as an intermediary between the top coat and the high-temperature alloy substrate. It enhances the bond strength between different structures and protects the metal substrate from oxidation [11]. Meanwhile, the top coat provides heat insulation and corrosion prevention, which are crucial for the overall high-temperature performance of the thermal barrier coating system [12].

Currently, the most widely used ceramic material is 6-8% yttrium oxide partially stabilized zirconia (YSZ), which has a low thermal conductivity, a high coefficient of thermal expansion (CTE), and a high fracture toughness, thus providing good performance in low-temperature engines [13]. However, for TBCs used in high-temperature, high-thrust-ratio, or high-load engines, YSZ is susceptible to phase change

*Corresponding author:
Tel : +86-159-4124-2356
E-mail: lz19870522@126.com

and sintering when the ambient temperature is higher than 1200 °C, making them unable to meet the more stringent requirements [14]. To improve the feasibility and coating performance of thermal barrier coatings in advanced engines, researchers have developed a series of new ceramic materials that take advantage of materials chemistry and rare earth chemistry. The development of these materials will provide an essential foundation for developing new TBCs [15].

The purpose of this paper is to review the advanced ceramic materials for thermal barrier coatings, including ZrO_2-based ceramic materials, $A_2B_2O_7$-type ceramic materials, rare-earth phosphates, rare-earth hafnates, yttrium aluminum garnet, perovskite oxides, magnetoplumbite compounds, high-entropy ceramics, rare-earth tantalates, rare-earth niobates, and rare-earth silicates. The existing problems and future development direction are also discussed.

ZrO_2-based ceramic materials

In industrial ceramics, ZrO_2 is widely utilized for its high fracture toughness, exceptional flexural strength, low thermal conductivity, and high coefficient of thermal expansion [16]. Pure ZrO_2 has three crystal structures: monoclinic phase (m-ZrO_2), tetragonal phase (t-ZrO_2), and cubic phase (c-ZrO_2) [17]. ZrO_2 exists only in the monoclinic phase at room temperature. When the temperature reaches about 1100 °C, it will be transformed into a tetragonal phase, and when heated to more than 2300 °C, it will be transformed into a cubic phase. The reversible phase transformation between these three phases is shown in Eq. (1) [18]:

$$\text{m-}ZrO_2 \underset{950°C}{\overset{1180°C}{\rightleftharpoons}} \text{t-}ZrO_2 \underset{2370°C}{\overset{2370°C}{\rightleftharpoons}} \text{c-}ZrO_2 \quad (1)$$

Due to the significant volume change during the transformation of m-ZrO_2 and t-ZrO_2, it is easier to cause the accumulation of stresses, which limits the application of pure ZrO_2 in high-temperature environments. Therefore, it is necessary to add different stabilizers to prepare ZrO_2 ceramics with different phase structures. Y_2O_3 is a kind of ZrO_2 stabilizer, and its content will affect the crystal structure of ZrO_2: when the mass fraction of Y_2O_3 is larger than 22%, ZrO_2 will be completely stabilized into cubic phase at room temperature, which is called yttrium oxide fully stabilized zirconia; when the mass fraction of Y_2O_3 is less than 22%, ZrO_2 will be stabilized into tetragonal phase (8-22%, mass fraction) or tetragonal-prime phase (6-8%, mass fraction) depending on the stabilizer content, which is called yttrium oxide partially stabilized zirconia [19]. In particular, 6-8% yttrium oxide partially stabilized zirconia has low thermal conductivity, high fracture toughness, and a high coefficient of thermal expansion, making it the most widely used material for TBCs at the present stage.

Although YSZ has excellent thermophysical properties, when the temperature is higher than 1200 °C, the t'-ZrO_2 will transform into the m-phase and c-phase through degradation and phase transformation. The transformation of ZrO_2 will cause volume expansion and create internal stress within the coating, which promotes the formation and expansion of cracks, allowing oxygen and corrosive materials to infiltrate, and accelerate corrosion in the thermal barrier coatings. In addition, the high sintering rate of YSZ in high-temperature environments reduces the porosity of the coating as well as phonon scattering, weakening the thermal insulation performance of the ceramic coat. Moreover, sintering increases the elastic modulus of the coating, decreases the crack stability, and accelerates the crack extension [20, 21]. Therefore, researchers added different rare earth oxides to YSZ to improve the high-temperature phase stabilization and other thermodynamic properties of TBC.

Single rare-earth oxide doped YSZ

The modification of YSZ by doping with rare-earth elements refers to the formation of multi-point dislocation effects, lattice distortions, and complementary effects by doping with rare-earth ions under the premise that the YSZ system remains unchanged, to achieve the purpose of inhibiting phase transformation, inhibiting sintering, improving thermal stability, improving corrosion resistance, and other thermophysical properties [22].

The element Sc has the smallest atomic mass and ionic radius among rare-earth elements, and has a similar electronic structure to the element Y. Therefore, Sc_2O_3 and Y_2O_3 have similar chemical properties and are often used in the doping modification of ZrO_2 ceramic materials. In addition, due to the similar ionic radius of Sc and Zr, it is easier to form replacement solid solutions and has a wider solid solution range. ScYSZ refers to YSZ doped with Sc_2O_3 as a stabilizer. Since the ionic radius of Sc is very small, doping in ZrO_2 does not cause significant lattice distortion, so researchers optimize the coating properties by adjusting the doping content of Sc_2O_3 [23]. Fan et al. [24] investigated the thermal shock life of ScYSZ coatings at 1300 °C when the Sc_2O_3 substance fraction was 7%. Although the doping of Sc elements decreased the fracture toughness slightly (4.3±0.3 $MPa \cdot m^{1/2}$), the excellent t' phase stability and higher comprehensive performance gave the TBCs a high thermal cycling life, reaching 2.6 times of the YSZ. Liu et al. [25] analyzed the phase composition of 8.0 mol% Sc_2O_3-YSZ coatings after heat treatment at 1500 °C for 10 h. Ultimately, the heat-treated ScYSZ thermal barrier coatings remained in a single tetragonal phase. In contrast, the substance amount fraction of the m phase in the YSZ coatings under the same conditions reached 49.4%. The excellent high-temperature phase stability enabled ScYSZ application in higher-temperature environments.

Gd_2O_3 has a weak covalent bond strength in rare-earth oxides, which can be used to achieve thermal conductivity

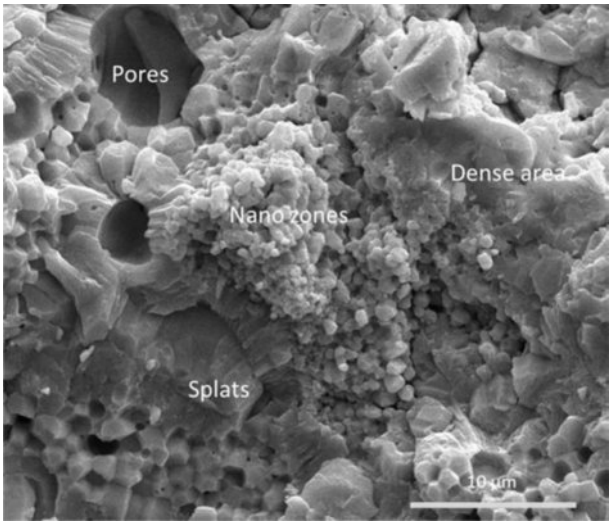

Fig. 1. SEM micrographs showing the cross-section of the fractured microstructure of as-sprayed GdYSZ coatings [27].

reduction by attenuating lattice vibrations [26]. The doping of Gd_2O_3 can also inhibit the grain growth of the top coat in a high-temperature environment, which enhances the anti-sintering property. Wang et al. [27] prepared nano-Gd_2O_3-modified YSZ TBCs using Air Plasma Spraying (APS). Fig. 1 shows the cross-sectional view of the fracture organization of GdYSZ, and it could be found that there were microstructures such as molten zone, nanoparticle zone, rod-like structure, nanopores, and microcracks inside the coatings. Compared with YSZ, the GdYSZ coating had more uniform particles, less crack content, and a denser organization, so the GdYSZ coating had a more excellent anti-peeling performance and thermal cycle life.

Jin et al. [28] prepared nano 4% Gd_2O_3-YSZ (4Gd-YSZ), nano 6% Gd_2O_3-YSZ (6Gd-YSZ), nano 8% Gd_2O_3-YSZ (8Gd-YSZ) coatings using APS, and compared the mechanical properties and thermal shock behavior with the nanostructured YSZ coatings. The results showed that the average hardness values of 4Gd-YSZ, 6Gd-YSZ, and 8Gd-YSZ were 532 $HV_{0.2}$, 532 $HV_{0.2}$, and 532 $HV_{0.2}$, respectively, which were lower than that of the nanostructured YSZ (553 $HV_{0.2}$); their bond strengths were 33 MPa, 30 MPa, and 28 MPa, respectively, which were also lower than that of the nanostructured YSZ (36 MPa). The tensile experiments showed significant differences between the failure behaviors of the YSZ and GdYSZ coatings. The weakest bond position in the YSZ coating was the interface between the TC and the BC, whereas the weakest position of the GdYSZ was inside the TC. The water-quenching lifetimes of nanostructured YSZ, 4Gd-YSZ, 6Gd-YSZ, and 8Gd-YSZ at 1100 °C were 33, 29, 24, and 17 cycles, respectively. When the doping amount of Gd_2O_3 was higher than 4%, it did not provide a good improvement in the mechanical properties of YSZ, and a large amount of doping would rather reduce the hardness and bond strength of the coating.

In summary, although adding a small amount of Gd_2O_3 to YSZ will improve the coating properties, the doping amount should be less than 4%. In addition, the research on nanostructured GdYSZ coating systems is limited, and their mechanical and thermal properties have not been fully investigated. If the performance of the YSZ coatings is to be significantly enhanced, a more suitable Gd_2O_3 ratio should be explored to enhance the mechanical properties of the coatings at high temperatures.

CeO_2 is widely used in oxygen storage materials, solid oxide fuel cells, catalytic industry, and water gas shift reactions [29]. In modification of TBC materials, CeO_2 is one of the most widely used rare-earth oxides. CeO_2 is a cubic crystal structure, which can be preferentially solid-solved in ZrO_2 with a large solid-solution interval (5-85%), and it can improve the high-temperature phase stability, coefficient of thermal expansion, thermal cycling performance, heat-insulating property, and corrosion-resistant property of YSZ [30]. In terms of high-temperature phase stability, Ce^{4+} increases the crowding of the ligating oxygen ions in t-ZrO_2 and exacerbates the dislocation deformation of the ligating oxygen ions in the C-axis direction [31, 32]. The stretching deformation of oxygen atoms causes a change in the spacing of Zr atoms and an increase in tetragonal properties. In addition, the significant difference in atomic radius and mass between the Ce and Zr produces a strong localized stress field, and the potential energy of the t→m phase transformation increases, inhibiting the m phase generation [33].

In terms of thermal insulation properties, Ce^{4+} has a higher atomic radius and relative mass, resulting in more significant lattice distortion caused by its doping substitution process. Yang et al. [32] investigated the thermal conductivity behavior of $[(ZrO_2)_{1-x}(CeO_2)_x]_{0.92}(Y_2O_3)_{0.08}$ ($0 \le x \le 1$) ceramics at different temperatures (Fig. 2). They discovered that the thermal conductivity of ceramic materials was lowest when x=0.3-0.5. In addition, the thermal conductivity of CeYSZ exhibited a higher temperature dependence, suggesting that the size difference between the different ions resulted in an inhomogeneous defect distribution. Although Ce^{4+} caused significant lattice defects, Ce^{4+} had the same valence as Zr^{4+}, and it was difficult to generate extra oxygen vacancies during the doping process, so the optimization of the thermal insulation properties of ceramic materials by single CeO_2 doping was limited.

In terms of thermal cycle life, CeO_2 doping can increase the coefficient of thermal expansion of the ceramics to 12.0×10^{-6} K^{-1}, which is higher than that of conventional YSZ ceramics, effectively reducing the thermal expansion mismatch stress between the coating, bond coat, and metal substrate. Lyu et al. [34] used nanoscale CeO_2 to modify YSZ thermal barrier coatings. They found that the incorporation of 1 mol% CeO_2 in YSZ was conducive to promoting the formation of microcracks inside the ceramic coat, releasing the coating stress, and slowing down the phase transformation from

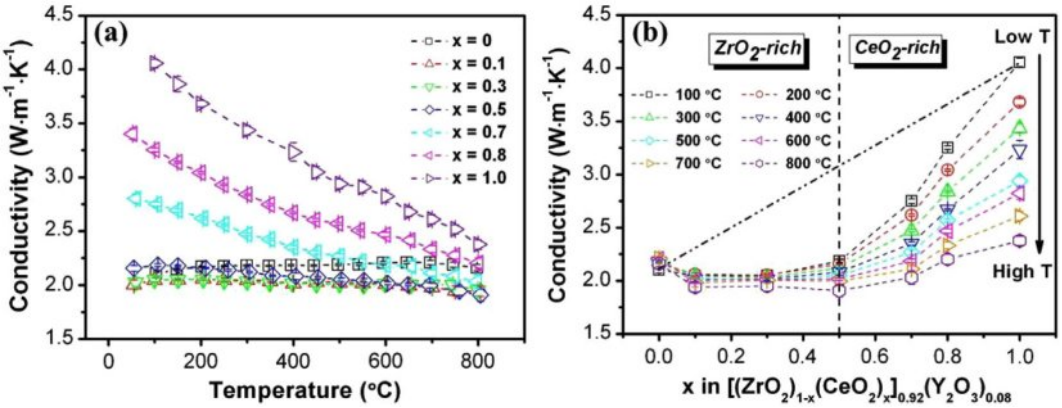

Fig. 2. (a) Thermal conductivities after zero porosity correction of the $[(ZrO_2)_{1-x}(CeO_2)_x]_{0.92}(Y_2O_3)_{0.08}$ ($0 \le x \le 1$) solid solutions at different temperatures, (b) Thermal conductivities of the $[(ZrO_2)_{1-x}(CeO_2)_x]_{0.92}(Y_2O_3)_{0.08}$ ($0 \le x \le 1$) solid solutions as a function of the composition x at different temperatures [32].

t-ZrO_2 to m-ZrO_2 during thermal shock.

Jin et al. [35] investigated the organization and thermal properties of APS 8%CeO_2-YSZ nanostructured coatings (CeYSZ). The results showed that the thermal cycle life of the CeYSZ at 1050 °C was 860 cycles, which was higher than that of conventional YSZ coatings (400 cycles) and nanostructured YSZ coatings (600 cycles). In addition, the thermal diffusion coefficients of the CeYSZ at 25-800 °C were 0.333-0.548×10^{-6} m^2/s, which were smaller than those of the conventional YSZ coatings (0.51-0.75×10^{-6} m^2/s) and nanostructured YSZ coatings (0.43-0.59×10^{-6} m^2/s). Venkadesan et al. [36] prepared CeO_2/8YSZ coatings on diesel engines and investigated their properties. The results showed that CeO_2 doping reduced the growth rate of TGO, significantly extended the lifetime of the coating, and decreased the thermal conductivity. In addition, CeO_2 doping facilitated the improvement of braking thermal efficiency of the diesel engine and reduced the fuel consumption.

CeYSZ has lower thermal conductivity, superior thermal cycle life, and better high-temperature phase stability than conventional YSZ. The performance of CeYSZ coatings is improved by adjusting the ratio of rare earth oxides and using multilayer nanostructures. In the future, if the performance of CeYSZ coatings is to be further improved, a more suitable CeO_2 doping ratio can be explored and combined with the optimization of the structural design and preparation process.

Zhao et al. [33] prepared SnYSZ ceramics by chemical co-precipitation and compared the lattice constants with conventional fluorite structural ceramics. The results are shown in Fig. 3. The doping of SnO_2 caused tetragonal distortion of the oxygen coordination in the t-phase and t' phase in YSZ, and stabilized the phase of ZrO_2 by the combined effect of lattice expansion and disordered structures. In terms of thermal conductivity, since Sn^{4+} has the same valence as Zr^{4+}, it does not generate extra oxygen vacancies during the doping process. Therefore, in SnYSZ, the phonon scattering mainly relies on

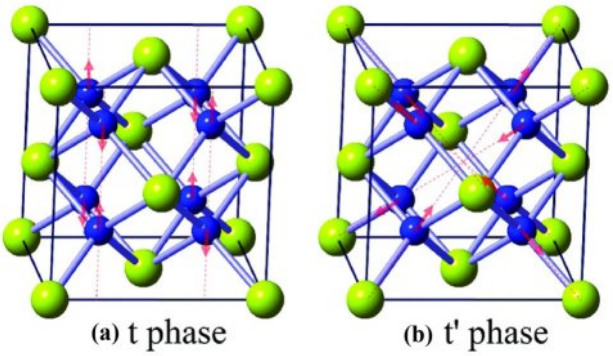

Fig. 3. Diagram of the lattice distortion for SnO_2-doped YSZ: (a) t phase, (b) t' phase [33].

the structural disorder caused by lattice distortion. In addition, SnO_2 forms $[SnO_4]^{4-}$ defect clusters during the doping process, which is favourable to reducing the phonon mean free path. Although SnO_2 improves the high-temperature phase stability of the material as well as its insulating properties, it decreases the coefficient of thermal expansion and the fracture toughness of the material. The decrease in the coefficient of thermal expansion is related to the substitution of Zr-O bonds by Sn-O bonds, which increases the lattice strength and decreases the coefficient of thermal expansion during the substitution process due to the higher covalent strength of Sn-O bonds. The decrease in fracture toughness is related to the weakening of the phase transformation toughening mechanism of ZrO_2, which requires more significant stress to induce the t→m phase transformation due to the increased t-phase stability of ZrO_2 by SnO_2 [37].

Multiple rare-earth oxide doped YSZ

Multiple rare-earth oxide doped YSZ coatings can retain the advantages of single rare-earth doping while compensating for the disadvantages of unit doping. Obtaining ceramic materials for TBCs with more excellent

comprehensive performance

YGYZ indicates YSZ doped with Yb_2O_3 and Gd_2O_3 as stabilizers. As one of the replacement materials of YSZ, YGYZ possesses better oxidation resistance, sintering resistance, high-temperature phase stability, and lower thermal conductivity than YSZ. In terms of thermal insulation properties, the thermal conductivity of YGYZ TBCs is about 0.85-1.24 $W \cdot m^{-1} \cdot K^{-1}$, which is only 60-70% of YSZ. This is attributed to the formation of extra oxygen vacancies by Gd^{3+} and Yb^{3+} ions in the substitution of Zr^{4+}, which enhanced the phonon scattering and reduced the thermal conductivity. In terms of corrosion resistance, Song et al. [38] analyzed the $Na_2SO_4+V_2O_5$ corrosion behavior of YGYZ coatings at 1100 °C. Since Gd_2O_3 and Y_2O_3 had high Lewis Alkali, they would preferentially participate in the corrosion process and consume the $NaVO_3$ molten salt. The least reactive Yb_2O_3 was retained to the end and stabilized the ZrO_2 to the t' phase. Finally, the YGYZ coating maintained a high t-phase ratio after thermal corrosion, and the degree of destabilization was only 40% of the YSZ coating. Although YGYZ exhibits outstanding corrosion resistance at high temperatures, its low fracture toughness (0.95-1.25 $MPa \cdot m^{1/2}$) and coefficient of thermal expansion (9-10×10^{-6} K^{-1}) prevent it from being prepared directly as a top coat on the surface of the bond coat. To improve the capability of YGYZ as the top coat material, Jung et al. [39] prepared a high-purity YSZ buffer coat between the nickel-based bond coat and the top YGYZ coat to reduce the thermal expansion difference and alleviate the mismatch stress, and the results showed that the YGYZ coatings with the high-purity YSZ buffer layer could reach 2000 cycles in the jet engine test, which is much higher than that of the no buffer layer 350-678 cycles for the coating without buffer coat.

Sun and Li et al. [40, 41] investigated the thermal properties of ScGd-YSZ coatings. The results showed that the ScGd-YSZ did not undergo a phase transformation after holding at 1400 °C for 500 h, and there was no t→m phase transformation during cooling. In addition, after Gd^{3+} and Sc^{3+} doping, a large number of oxygen vacancies were introduced due to the valence differences, and the differences in the mass and radius of Gd^{3+}, Sc^{3+}, Zr^{4+}, and Y^{3+} further reduced the thermal conductivity. Among them, when the molar fractions of both Sc_2O_3 and Gd_2O_3 were 3.7%, ScGd-YSZ had the lowest thermal conductivity of 1.21-1.32 $W \cdot m^{-1} \cdot K^{-1}$, which was 40% lower than that of the conventional YSZ coatings.

Guo et al. [42] investigated the effect of co-doping of Re_2O_3 (Re=La, Nd, and Gd) and Yb_2O_3 on the thermal properties of YSZ coatings. The results showed that the doping of multi-component rare-earth oxides was favorable to reduce the decomposition drive of the t' phase, and the phase stability and thermal conductivity increased with the decrease of the atomic radius of the dopant elements.

YSZ doped by other materials

$MoSi_2$ is a ceramic material with a high melting point, good thermal shock resistance, low coefficient of thermal expansion, and excellent oxidation resistance [43]. Researchers recognize $MoSi_2$ as a potential self-healing material for TBCs with promising applications. The self-healing behavior of $MoSi_2$ in TBCs is related to its unique crystal structure. $MoSi_2$ is a typical Daltonian intermetallic compound with two special crystalline structures, $C11_b$-type and C40-type, thus possessing both metallic and ceramic properties [44, 45]. The oxidation behavior of $MoSi_2$ in thermal barrier coatings shows stage differences with the change of ambient temperature [46, 47]: (1) In the first stage (400-800 °C), the diffusion coefficient of $MoSi_2$ is low, so MoO_3 and SiO_2 are formed during this oxidation process, but the content of SiO_2 is not enough to create a dense layer with the protective effect, and it can't sufficiently repair internal defects of the ceramic coat; (2) In the second stage (800-1200 °C), due to the increase in temperature, $MoSi_2$ will be oxidized to form Mo_5Si_3, MoO_3, and SiO_2; (3) In the third stage (≥1200 °C), $MoSi_2$ will be oxidized to Mo_5Si_3 and SiO_2, which forms a dense and continuous SiO_2 protective layer on the surface of the material and fills the small cracks inside the ceramic coat, effectively inhibiting the expansion and bridging of the cracks inside the ceramic coat.

Kulczyk-Maleka et al. [48] prepared $MoSi_2$-modified YSZ ceramics by spark plasma sintering (SPS) and characterized the thermomechanical properties. The results showed that the thermal expansion coefficient of 20 vol.% $MoSi_2$-YSZ ceramics was similar to that of conventional YSZ, so doping $MoSi_2$ powder would not increase the thermal expansion mismatch stress inside the thermal barrier coatings. In addition, $MoSi_2$ powder did not affect the fracture toughness of YSZ ceramics. Yu et al. [47] designed and prepared three kinds of YGYZ TBCs with different $MoSi_2$ doping contents, including 10%$MoSi_2$-YGYZ (Mo10), 20%$MoSi_2$-YGYZ (Mo20), 30%$MoSi_2$-YGYZ (Mo30). The results showed that all the coatings were t-ZrO_2 and t-$MoSi_2$ phases and had a well-bonded layered structure. In terms of antioxidant behavior, the oxidized weight gain and TGO thickness of Mo20 coatings were the smallest, which were 3.9 $mg \cdot cm^{-2}$ and 3 μm respectively.

SiC fibers are considered to be a structure/functionally integrated material due to their low density, high mechanical strength, excellent high-temperature resistance, and anti-oxidant properties [49]. In thermal barrier coatings, SiC fibers are used to improve the fracture toughness of ceramic coats. Fig. 4 shows the schematic diagram of the SiC fibers toughening principle [50]. The SiC fibers in the ceramic coat create new surfaces and consume large amounts of energy during the processes of debonding, pull-out, and fracture [51]. At the same time, the "bridging" phenomenon inhibits the crack expansion, effectively limiting the growth and spread of cracks in

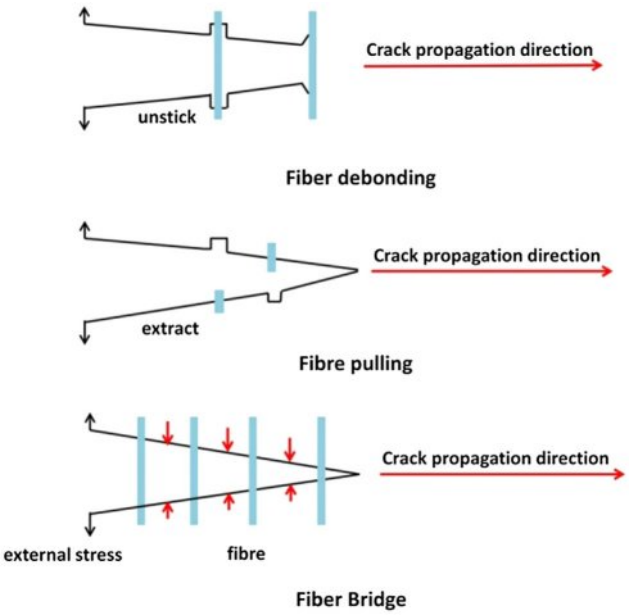

Fig. 4. Schematic diagram of fiber toughening principle [50].

the coating at alternating temperatures during thermal cycling. In addition, the deflection of cracks produces a significant toughening effect on the thermal barrier coatings. Due to the differences in physical properties, such as the coefficient of thermal expansion and modulus of elasticity between the fibers and the ceramic coat, a stress field is generated around the fibers. The stress field makes it difficult for the cracks to pass through the fibers during expansion, which deflects and consumes a lot of energy, significantly enhancing the fracture toughness of the YSZ coating [52].

Fang et al. [53] prepared SiC fiber/YSZ TBCs by APS and characterized the mechanical properties of the modified coatings. The results showed that the thermal cycle life and fracture toughness of the SiC fiber/YSZ TBCs were 442±13 cycles and 1.54 MPa·$m^{1/2}$ respectively, which were 1.6 times and 1.3 times higher than those of the conventional TBCs. Ma et al. [54] prepared SiC fiber/YSZ composite thick thermal barrier coatings by APS. Due to the "reinforced concrete frame structure" of SiC fibers in the thick ceramic coats, the fracture toughness of the thick thermal barrier coatings reached 1.67 MPa·$m^{1/2}$, which was higher than the average value of the conventional YSZ coatings. Cheng et al. [55] prepared SiC whisker-toughened YSZ thermal barrier coatings by APS and characterized their microscopic morphology and thermal cycle life. The results showed that the SiC whiskers were structurally intact and uniformly distributed inside the ceramic layer during the thermal spraying process. The thermal cycle life of the whisker-toughened thermal barrier coating reaches 136.3 cycles, which is 1.02 times higher than that of the conventional YSZ TBCs.

Currently, reinforcement phases such as whiskers and fibers provide an effective method to optimize the high-temperature fracture toughness of thermal barrier coatings, and improve the toughness as well as the mechanical stability of the ceramic coat by compositing high-strength fibers with the material. However, fiber toughening does not optimize the modification of the coating substrate material, so the strengthening effect is limited to the thermodynamic properties. In addition, more in-depth research is needed on the effect of fiber reinforcement on the thermal corrosion behavior of thermal barrier coatings to explore the optimization mechanism of fiber type, doping content, and preparation method on thermal barrier coatings.

$A_2B_2O_7$-type ceramic materials

In the 1960s, Fu-k'ang et al. [56] first reported the $A_2B_2O_7$-type ceramics. During its development, it was applied to thermal barrier coatings, luminescence powders, photocatalysts, and so on [57-60]. The A-site in $A_2B_2O_7$-type ceramics is generally a trivalent rare-earth element, and the B-site is generally a tetravalent transition metal element. The crystal structure of $A_2B_2O_7$-type ceramics is affected by temperature, pressure, and the radius ratio of the A-site and B-site atoms [61]. Among them, the radius ratio of the A-site and B-site atoms is the dominant factor. When $1.46<r_A/r_B<1.78$ is an ordered pyrochlore structure; When $r_A/r_B<1.46$, it is a fluorite structure; When $r_A/r_B>1.78$, it is generally a monoclinic structure [62]. The fluorite structure has a

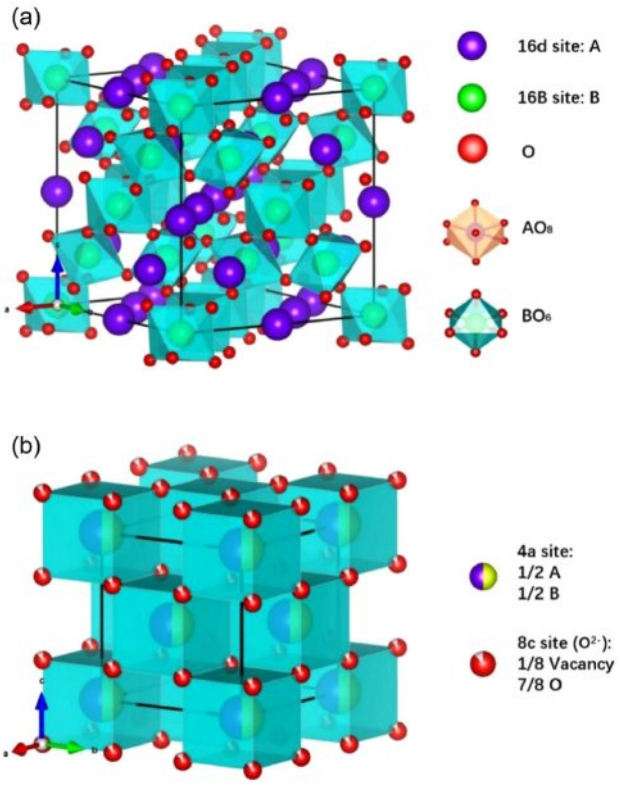

Fig. 5. The crystal structure for (a) pyrochlore-type and (b) defective fluorite-type $A_2B_2O_7$ [63].

disordered arrangement of A-site and B-site atoms, while the pyrochlore structure has an ordered arrangement of A-site and B-site atoms.

The crystal structures of $A_2B_2O_7$-type ceramics with pyrochlore structure and defective fluorite structure are shown in Fig. 5 [63]. The ideal pyrochlore structure is a superstructural derivative of the AO_2-type fluorite structure, where the A-site and B-site cations are ordered along the <111> direction and no one-eighth oxygen vacancies exist. The pyrochlore structure $A_2B_2O_7$-type ceramics can be written as $A_2B_2O_6O'$ ($Fd\bar{3}m$ space group), and the A, B, O, O' ions occupy 16c, 16d, 48f, and 8b four crystalline sites, respectively [64]. The defective structure of fluorite exhibits the $Fm\bar{3}m$ space group, causing disorder in the arrangement of cations and distribution of oxygen vacancies [65]. Currently, $A_2B_2O_7$-type ceramics applied to thermal barrier coatings mainly include rare-earth zirconates and rare-earth cerium oxides.

Rare-earth zirconates

Rare-earth zirconates are the most widely used $A_2B_2O_7$-type ceramics, and the crystal structure is highly related to the type of rare-earth ions. If the rare-earth element has a large ionic radius and relative atomic mass, it combines with zirconate ions to form pyrochlore; If the rare-earth element has a small radius and a large relative atomic mass, it combines with zirconate ions to form a defective fluorite structure [66].

In terms of thermal conductivity, rare-earth zirconate materials, both pyrochlore and defective fluorite structures, have intrinsic oxygen vacancies in each crystal structure unit, with a high concentration of oxygen vacancies and the presence of rare-earth atoms of larger mass in the crystal cell, which enhances the phonon scattering effect and leads to a decrease in the phonon mean free path, so that this type of material has a low thermal conductivity [67]. Bobzin et al. [68] analyzed the thermal conductivities of LZO and 8YSZ at 1000-1300 °C ambient temperature, and the results showed that the thermal conductivity of LZO fluctuates with the increase of ambient temperature, but it was still smaller than that of 8YSZ. Xu et al. [69] prepared $Dy_2Zr_2O_7$ ceramics with defective fluorite structure by solid-state reaction method and characterized their coefficient of thermal expansion as well as thermal conductivity. The results showed that $Dy_2Zr_2O_7$ had a higher coefficient of thermal expansion with lower thermal conductivity compared with YSZ. Wu et al. [70] measured the thermal conductivities of $Gd_2Zr_2O_7$, $Nd_2Zr_2O_7$, $Sm_2Zr_2O_7$, and YSZ, and the results showed that all $A_2Zr_2O_7$-type ceramics had lower thermal conductivities than YSZ (Table 1).

Table 1. Thermal conductivity and coefficient of thermal expansion of different materials [69, 70].

Materials	Thermal Conductive ($W \cdot m^{-1} \cdot K^{-1}$)	Coefficient of Thermal Expansion ($\times 10^{-6}$ K^{-1})
YSZ	2.3 (700 °C)	11 (1000 °C)
$La_2Zr_2O_7$	1.3 (1100 °C)	9.1 (1000 °C)
$Gd_2Zr_2O_7$	1.6 (700 °C)	11.6 (1200 °C)
$Sm_2Zr_2O_7$	1.5 (700 °C)	10.8 (1200 °C)
$Dy_2Zr_2O_7$	1.34 (800 °C)	11.1 (1200 °C)

To further improve the thermal insulation properties and coefficient of thermal expansion of single rare-earth zirconate ceramics, doping modification has become a major research direction. Since heat transfer in the high-temperature range mainly depends on phonon interactions, and phonon thermal conductivity is related to lattice scattering. By introducing defects through doping, the phonon scattering can be enhanced, and the material's thermal conductivity can be reduced. In addition, doping-introduced defects can reduce the lattice energy, which serves to increase the coefficient of thermal expansion [71].

Gok et al. [72] modified $La_2Zr_2O_7$ ceramics using Gd^{3+} and Yb^{3+} doping, respectively, and the thermal conductivities of the two modified ceramics were 0.38-0.68 $W \cdot m^{-1} \cdot K^{-1}$, which were much lower than those of

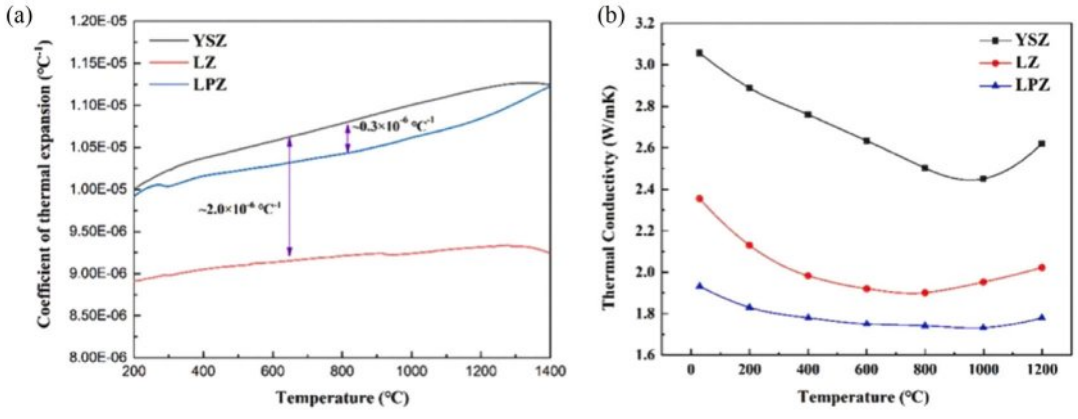

Fig. 6. Thermal properties of LPZ ceramics (a) Coefficient of thermal expansion of YSZ, LZ, and LPZ, (b) YSZ, LZ, and LPZ materials thermal conductivity with the temperature variation [73].

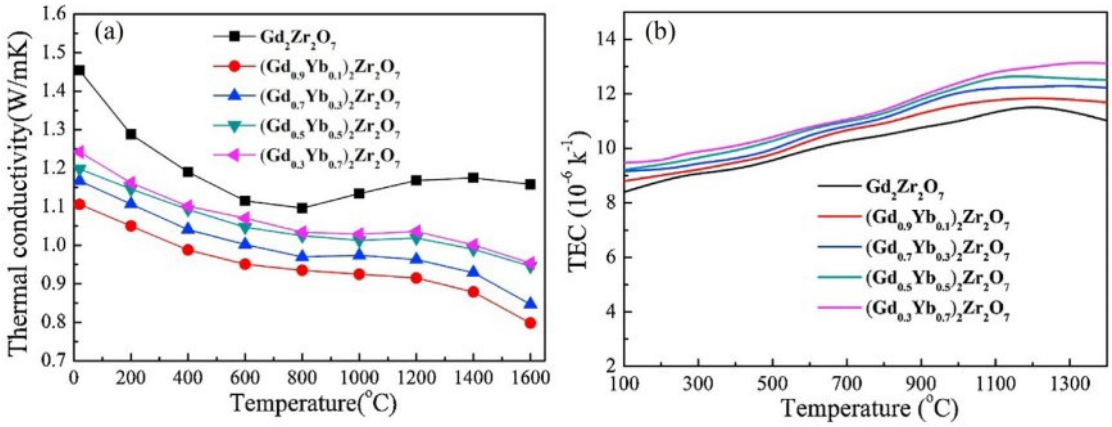

Fig. 7. (a) Thermal conductivities of $(Gd_{1-x}Ybx)_2Zr_2O_7$ (x = 0, 0.1, 0.3, 0.5, 0.7) ceramics, (b) CTEs of $(Gd_{1-x}Yb_x)_2Zr_2O_7$ (x = 0, 0.1, 0.3, 0.5, 0.7) ceramics [74].

the conventional YSZ (0.88-1.00 $W \cdot m^{-1} \cdot K^{-1}$). Liu et al. [73] investigated the thermophysical properties of Pr-doped $La_2Zr_2O_7$ (LPZ) ceramics and compared them with conventional LZO and YSZ. The results are shown in Fig. 6. The thermal expansion coefficients of LPZ ceramics were 9.8-11.2×10^{-6} K^{-1}, which were higher than those of conventional LZO ceramics and close to those of YSZ ceramics. Pr element doping increased point defects in the LZO crystal structure and led to excessively relax the crystal lattice. In addition, the thermal conductivity of LPZ ceramics was only 1.7-2.0 $W \cdot m^{-1} \cdot K^{-1}$, much lower than that of conventional LZO and YSZ ceramics. The lower thermal conductivity of LPZ ceramics was related to point defects and lattice distortions caused by Pr during the doping process, and the disordered structure increased the chances of phonon expansion, thus reducing the phonon mean free path.

Guo et al. [74] synthesized $(Gd_{1-x}Yb_x)_2Zr_2O_7$ ceramics with optimized thermophysical properties by doping different contents of Yb_2O_3, and the thermal conductivity of the doped ceramic material was 0.80±0.02 $W \cdot m^{-1} \cdot K^{-1}$, which was 20% lower than that of $Gd_2Zr_2O_7$ (Fig. 7(a)). The decreased thermal conductivity was mainly due to the difference in mass, size, and interatomic bond strength between Yb^{3+} and Gd^{3+} ions, which enhanced the scattering of phonons through mass and strain fluctuations and decreased the phonon mean free path, leading to a decrease in thermal conductivity. In addition, the thermal expansion coefficient of $(Gd_{1-x}Yb_x)_2Zr_2O_7$ ceramics increased with the increase of Yb_2O_3 doping content, which was higher than that of $Gd_2Zr_2O_7$ and YSZ ceramics at the same temperature (Fig. 7(b)). The change in the coefficient of thermal expansion was mainly due to the introduction of defects by doping, which enhanced the anharmonic vibrations of the lattice, thus increasing the coefficient of thermal expansion.

Although LZO possesses excellent thermal insulation, high-temperature phase stability, and sintering resistance, its poor fracture toughness limits its application in complex environments. Therefore, it is important to study and improve the thermodynamic properties of LZO.

Jin et al. [75] doped $La_2Zr_2O_7$ using YSZ fibers and Multi-Walled Carbon Nanotubes (MWCNTs), respectively. Fig. 8 shows the microscopic morphology of the two doped powders. The doped YSZ fibers existed independently on the exterior of the spherical particles, while the MWCNTs were attached to the particle surface. The results showed that the bonding strength of the YSZ fibers coatings could be increased to 1.84 times of the undoped coating; however, the bond strength of the MWCNTs coatings did not increase significantly.

Rare-earth cerium oxides

Rare-earth cerium oxides with fluorite structure are the solid solutions generated by the dissolution of rare-earth oxides in the CeO_2 lattice. Rare-earth cerium

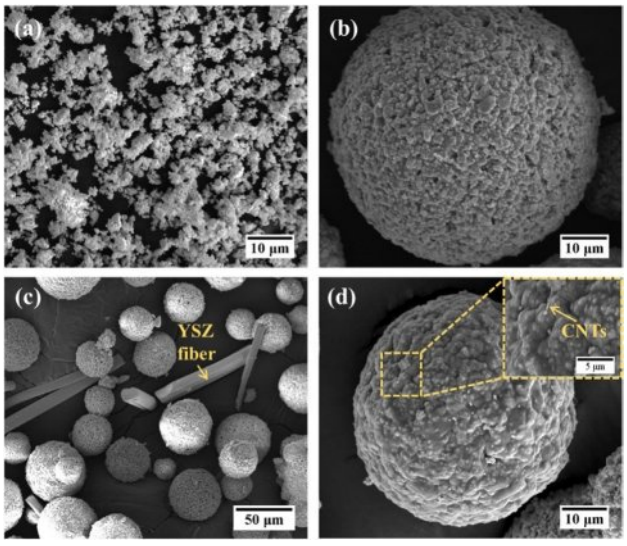

Fig. 8. The high magnification images of (a) $La_2Zr_2O_7$ particles after crushing, (b) $La_2Zr_2O_7$ powders after spray granulation, (c) $La_2Zr_2O_7$-YSZ fibers mixed powders, and (d) $La_2Zr_2O_7$-MWCNTs powders [75].

oxides have a low thermal conductivity due to the low thermal conductivity of CeO_2 and the large number of oxygen vacancies present in the fluorite structure [76, 77]. In addition, rare-earth cerium have high chemical stability, thermal shock resistance, and low oxygen ion conductivity at 2000 °C. In 2003, Cao et al. [78] first reported the application of $La_2Ce_2O_7$ (LCO) in thermal barrier coatings, and the thermal conductivity of $La_2Ce_2O_7$ was only 0.6 $W \cdot m^{-1} \cdot K^{-1}$ at 1000 °C, which was much lower than that of conventional YSZ ceramics. In addition, the lattice energy of the system decreased due to the reduction of Ce^{4+} to Ce^{3+} in a high-temperature environment. According to the "Boon Langde lattice theory", the reduction of lattice energy was conducive to the improvement of the thermal expansion coefficient of ceramic materials, so the LCO ceramics could reach a coefficient of thermal expansion of 14.0×10^{-6} K^{-1}. Yu et al. [79] prepared $Dy_2Ce_2O_7$ and $Y_2Ce_2O_7$ by solid-state reaction method, and the thermal conductivities of the two ceramics at 800 °C were 1.82 $W \cdot m^{-1} \cdot K^{-1}$ and 1.78 $W \cdot m^{-1} \cdot K^{-1}$, respectively, which were 20% lower than that of the traditional YSZ.

By doping the rare-earth cerium oxides with one or more rare-earth elements, it can improve the service properties of the coating, reduce thermal conductivity, and increase the coefficient of thermal expansion. Zhang et al. [80] prepared two modified ceramics $(La_{0.7}Gd_{0.3})_2Ce_2O_7$ and $(La_{0.9}Gd_{0.1})_2Ce_2O_7$ by solid-state reaction method and compared the coefficient of thermal expansion as well as thermal conductivity with $La_2Ce_2O_7$. The results showed that both modified ceramics had higher coefficients of thermal expansion and lower thermal conductivity, and the thermal conductivity decreased with the increase of Gd^{3+} content. Shao et al. [81] prepared $(Sm_{0.5}La_{0.5-x}Nd_x)_2Ce_2O_7$ (x=0, 0.2, and 0.4) coatings with different Nd^{3+} and La^{3+} doping content, and compared the thermal conductivity and thermal expansion coefficient with conventional $Sm_2Ce_2O_7$. The results showed that due to the significant difference in ionic radius and relative atomic mass of the dopant elements, it increased the internal defects of the ceramic lattice, provided extra space for phonon scattering, and reduced the thermal conductivity of the coatings. The thermal conductivity of the three modified coatings at 1000 °C was 1.32-1.58 $W \cdot m^{-1} \cdot K^{-1}$, which was much lower than that of the conventional $Sm_2Ce_2O_7$. In terms of the coefficient of thermal expansion, since the ionic radius of both La and Nd is larger than Sm, the lattice energy of the solid solution decreases gradually with the increase of the elemental doping content, which leads to the increase of its coefficient of thermal expansion with the increase of the elemental doping content of La.

Although rare-earth cerium oxides have excellent thermal insulation properties and high coefficients of thermal expansion, the preparation of rare-earth cerium oxide coatings with rated stoichiometric ratios is a significant challenge for the development and application of this material [82]. During plasma spraying, 30-40% of CeO_2 in rare-earth cerium oxide coatings will be lost, resulting in a lower coating deposition rate. Therefore, an additional increase of CeO_2 content is required to obtain a rare-earth cerium oxide coating with a standard stoichiometric ratio in the preparative state, and subtle compositional shifts in CeO_2 can significantly affect the coating's service properties. Ma [83] conducted thermal cycling tests on thermal barrier coatings with three powder doping ratios of $La_2O_3 \cdot 3.0CeO_2$ (LC3), $La_2O_3 \cdot 3.25CeO_2$ (LC3.25), and $La_2O_3 \cdot 3.5CeO_2$ (LC3.5), and found that compositional shifts severely affected the thermal cycling lifetimes of rare-earth cerium oxide coatings. The lifetime of LC3.25 reached 3238 cycles at 1230°C, while the lifetime of LC3 and LC3.5 was 847 and 50 cycles, respectively.

Rare-earth phosphates

The chemical formula of rare-earth phosphate is $RePO_4$, which exists in two main structures: the monazite structure and the xenotime structure [84]. When Re is a light rare-earth element with a large ionic radius (Re=La-Gd), $RePO_4$ is a monazite structure (Fig. 9(a)), including $[PO_4]$ polyhedra and $[ReO_9]$ polyhedra; when Re is a heavy rare earth element with a small ionic radius (Re=Tb-Lu, and Y), $RePO_4$ is a xenotime structure (Fig. 9(b)), including $[PO_4]$ polyhedra and $[ReO_8]$ polyhedra [85]. Due to the high thermal conductivity and low coefficient of thermal expansion of rare-earth phosphates with xenotime structure, they are not suitable to be used as ceramic materials for thermal barrier coatings. In contrast, the monazite structured rare-earth phosphates with high coefficients of thermal expansion as well as low thermal conductivities are considered to be ceramic materials for thermal barrier coatings with good application prospects [86].

Lanthanum phosphate ($LaPO_4$) is one of the most widely researched and applied materials among monazite-structured rare-earth phosphates, with a high melting point (2070 °C), low thermal conductivity,

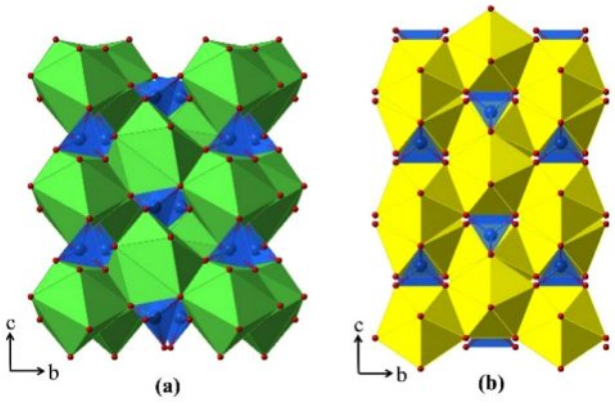

Fig. 9. Crystal structure of $RePO_4$: (a) monazite, (b) xenotime [85].

excellent high-temperature phase stability, and good high-temperature resistance to sulfur and vanadium corrosion [87]. However, if the top coat of $LaPO_4$ is prepared directly on the bond coat, the weak bond strength will cause the ceramic coat to fall off rapidly in high-temperature environments. Therefore, the structural design of lanthanum phosphate coatings is needed to improve their high-temperature usability. Zhang et al. [88] prepared $LaPO_4$-YSZ double-layer TBCs by APS and analyzed the failure mechanism of the double-layer coatings. The results showed that the cracks appeared inside the top coat of $LaPO_4$ led to the coating peeling off, while the excellent bond strength between the layers indicated that the double-layer structural coatings could improve the bond strength between the $LaPO_4$ coatings and the bond coats. In addition, the corrosion products of the double-layer coatings in different temperature V_2O_5 corrosive environments were analyzed. The corrosion products were La(P, V)O4 at 700-900 °C, and a small amount of $LaVO_4$ appeared in the corrosion products at 1000 °C. Since La(P, V)O_4 did not adversely affect the microstructure of the coatings, it indicated that the $LaPO_4$, as a top coat of the thermal barrier coatings, had excellent V_2O_5 corrosion resistance.

$LaPO_4$ can be used not only as a top coat ceramic material but also for the modification of ceramic coating. Yang et al. [89] found that $LaPO_4$ doping into $La_2Zr_2O_7$ forms a percolating interconnected network, which significantly reduces the infrared radiation transmittance in the sample. When $LaPO_4$ doping was 20% (mass fraction), the fracture toughness of $La_2Zr_2O_7$ ceramic materials was increased and the elastic modulus was decreased, which was favorable for the engineering applications of $LaZr_2O_7$ materials. Li et al. [90] prepared nanostructured 30 mol.% $LaPO_4$ doped $Gd_2Zr_2O_7$ thermal barrier coatings by APS and characterized the corrosion resistance behavior at 1250 °C. The thermal corrosion results showed that $LaPO_4$ could promote the formation of Gd-La-P apatite, which led to the formation of a dense crystalline reaction layer on the surface of the coatings, effectively preventing the penetration of molten CMAS, and improved the high-temperature corrosion resistance of the thermal barrier coatings.

Rare-earth hafnates

Rare-earth hafnates as a new ceramic material for thermal barrier coatings, have a higher melting point than rare-earth zirconates and superior phase stability, thus allowing them to be used in higher-temperature environments. From Fig. 10 [91], it can be seen that rare-earth hafnates can form many types of compounds depending on the rare-earth element. Rare-earth elements with large ionic radius (Re=La-Gd) can form $Re_2Hf_2O_7$ with a pyrochlore structure; Rare-earth elements with smaller ionic radius (Re=Ho-Lu, and Sc) can form $Re_4Hf_3O_{12}$ with a δ structure. Among them, part of the

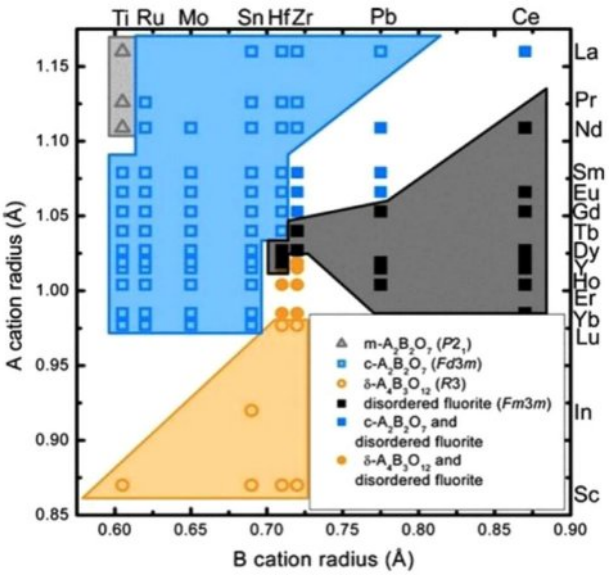

Fig. 10. Composition and structure of $A^{3+}{}_mB^{4+}{}_nO_{3m/2+2n}$ compounds [91].

pyrochlore $Re_2Hf_2O_7$ and δ-$Re_4Hf_3O_{12}$ undergoes an ordered-disordered transition from an oxygen vacancy-ordered structure to an oxygen vacancy-disordered structure in a high-temperature environment [92].

The Re_2O_3-HfO_2 system can form defective fluorite structure-derived compounds MO_{2-x}, and the structure of MO_{2-x} has a fluorite-like structure. The oxide fluorite MO_2 with an ideal stoichiometric ratio has a face-centered cubic structure, and to form a defective fluorite structure with oxygen vacancies, M^{4+} in MO_2 will be replaced by cations with different valence states and charge balance will be achieved by introducing extra oxygen vacancies [93].

$A_2Hf_2O_7$

$A_2Hf_2O_7$-type ceramics have a pyrochlore-like structure with a special arrangement of defects, such as ions and vacancies, unique to the structure, which leads to favorable properties, such as low thermal conductivity, high coefficient of thermal expansion, and good high-temperature phase stability.

Du et al. [94] prepared $Y_2Hf_2O_7$ ceramics with pyrochlore structure by solid-state reaction method and compared the thermal conductivity with conventional YSZ. When Y_2O_3 was doped with HfO_2, an ion substitution phenomenon would occur, and oxygen vacancies would be generated in the lattice to maintain the electroneutrality of the lattice, and the oxygen vacancies increased with the increase of the doping content of rare earth oxides. The content of Y_2O_3 in 7YSZ was only 3.5 mol%, while the content of Y_2O_3 in $Y_2Hf_2O_7$ was 33 mol%. As a result, the $Y_2Hf_2O_7$ crystals had more oxygen vacancies than the 7YSZ crystals, leading to enhanced phonon scattering due to the oxygen vacancies, which resulted in $Y_2Hf_2O_7$ (0.6-0.8 $W \cdot m^{-1} \cdot K^{-1}$) having a lower thermal

conductivity than 7YSZ. Yang et al. [95] synthesized pyrochlore-type $Gd_2Hf_2O_7$ ceramics and characterized their thermophysical properties. The results showed that the thermal conductivity of $Gd_2Hf_2O_7$ ceramics at 1200 °C was 1.40 $W \cdot m^{-1} \cdot K^{-1}$, which was 25% lower than that of conventional 8YSZ. In addition, the $Gd_2Hf_2O_7$ ceramics exhibited a large thermal expansion coefficient, higher than that of the conventional 8YSZ. Liang et al. [96] prepared a pyrochlore-structured $La_2Hf_2O_7$ ceramic with excellent phase stability, and the thermal conductivity of this ceramic at 1000 °C was only 1.34 $W \cdot m^{-1} \cdot K^{-1}$, which was about 40% lower than that of conventional 8YSZ ceramics. However, the thermal expansion coefficient of the $La_2Hf_2O_7$ ceramic was only 8.76×10^{-6} K^{-1}, so a dual-layer structure design was required for the coating design. Sun et al. [97] investigated the structure and properties of $Re_2Hf_2O_7$ ceramics by first-principles calculations. The results showed that all $Re_2Hf_2O_7$ ceramics had a pyrochlore structure, and the lattice parameters of these pyrochlores increased with the Re radius increasing in the order from Sm to La. The predicted thermal conductivities at 1600 K are 1.38 $W \cdot m^{-1} \cdot K^{-1}$ for $La_2Hf_2O_7$, 1.56 $W \cdot m^{-1} \cdot K^{-1}$ for $Ce_2Hf_2O_7$, 1.60 $W \cdot m^{-1} \cdot K^{-1}$ for $Pr_2Hf_2O_7$, 1.62 $W \cdot m^{-1} \cdot K^{-1}$ for $Nd_2Hf_2O_7$, 1.63 $W \cdot m^{-1} \cdot K^{-1}$ for $Pm_2Hf_2O_7$, and 1.62 $W \cdot m^{-1} \cdot K^{-1}$ for $Sm_2Hf_2O_7$. All these values were lower than the thermal conductivity of YSZ.

$A_4Hf_3O_{12}$

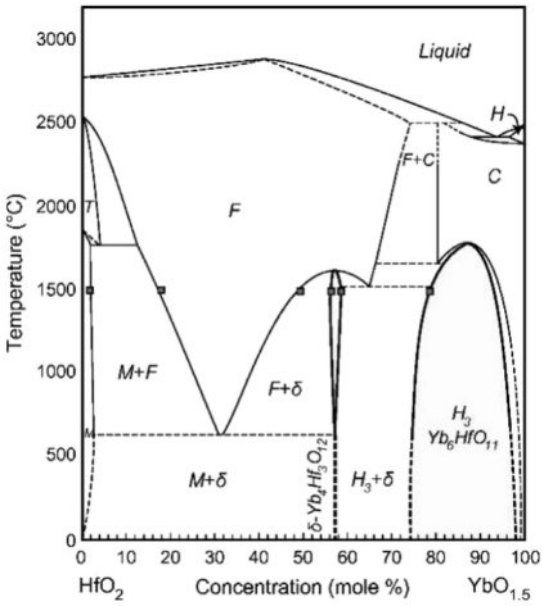

Fig. 11. Phase diagram for the pseudobinary system HfO_2-$YbO_{1.5}$ [101, 102].

For the δ-$A_4B_3O_{12}$ oxides, the ionic size of the cation A^{3+} ranges from Sc^{3+} to Ho^{3+}, and the cation B^{4+} ranges from Ti^{4+} to Zr^{4+} [98]. Throughout the compositional range, part of δ-$A_4B_3O_{12}$ undergoes an ordered-disordered transition from δ-$A_4B_3O_{12}$ to $A_4B_3O_{12}$ with a disordered fluorite structure in a high-temperature environment.

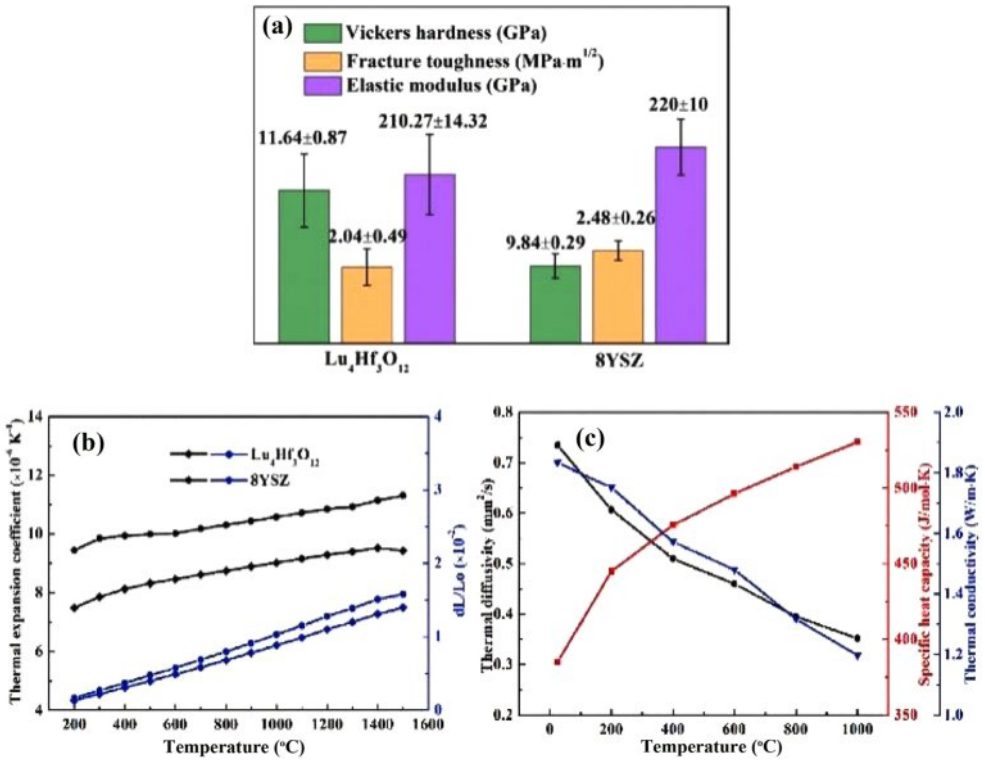

Fig. 12. (a) Mechanical properties of the $Lu_4Hf_3O_{12}$ ceramic, compared with those of the traditional 8YSZ bulk, (b) Thermal expansion behavior of the $Lu_4Hf_3O_{12}$ ceramic versus the temperature, compared to the traditional 8YSZ ceramics, (c) Specific heat capacity, thermal diffusivity and thermal conductivity of the $Lu_4Hf_3O_{12}$ ceramic [105].

Bogicevic et al. [99, 100] predicted the ordered cationic structures of δ-$Y_4Zr_3O_{12}$ and δ-$Sc_4Zr_3O_{12}$ using density-functional theory. The cationic arrangement of $Y_4Zr_3O_{12}$ was predicted by calculating the lattice energies of 45 different configurations of 19 protocells. For the ordered structure of $Y_4Zr_3O_{12}$, it was calculated that position 3*a* was completely occupied by $Zr^{4+,}$ and position 18*f* was occupied by Y^{3+} and Zr^{4+} in an ordered arrangement.

Duan and Poerschke et al. [101, 102] mapped the HfO_2-Yb_2O_3 phase diagram and confirmed that the transformation of the ordered phase δ-$Yb_4Hf_3O_{12}$ to a disordered fluorite structure occurs at a temperature of about 1580 °C (Fig. 11). Karaulov et al. [103] prepared $Yb_4Hf_3O_{12}$ and $Gd_4Hf_3O_{12}$ in their study of the ZrO_2-HfO_2-Gd_2O_3 and ZrO_2-HfO_2-Yb_2O_3 systems, and the two ceramics had a lower thermal conductivity than the rare-earth zirconates.

Rare-earth hafnates are considered candidate materials for future thermal/environmental barrier coatings for engines due to their higher melting points and superior high-temperature phase stability compared to rare-earth zirconates. In addition, since $Re_4Hf_3O_{12}$ has more rare earth elements than $Re_2Hf_2O_7$, it is expected to provide superior corrosion resistance.

Ueno et al. [104] investigated the water vapor corrosion behavior of $Lu_4Hf_3O_{12}$ ceramics in a 1500 °C environment. The results showed that the $Lu_4Hf_3O_{12}$ phase exhibited excellent water vapor corrosion resistance with a weight loss rate of only 1.347×10^{-6} g/cm^{2}h, which was of the same order of magnitude as the water vapor corrosion rates of $Lu_2Si_2O_7$ and mullite. Lue et al. [105] prepared $Lu_4Hf_3O_{12}$ ceramics by solid-state reaction method and characterized their thermophysical properties. The results are shown in Fig. 12. The fracture toughness and elastic modulus of $Lu_4Hf_3O_{12}$ ceramics were 2.48±0.26 MPa·m$^{1/2}$ and 210.27±14.32 GPa, respectively, which were similar to those of conventional YSZ ceramics. The coefficient of thermal expansion of $Lu_4Hf_3O_{12}$ ceramics was 8.46×10^{-6} K^{-1}, and the lower coefficient of thermal expansion was conducive to reducing the thermal expansion mismatch stresses within the coating when $Lu_4Hf_3O_{12}$ was applied to the environmental barrier coatings; However, a dual-ceramic-layer design was required to optimize the coating thermal cycling life when $Lu_4Hf_3O_{12}$ was applied to the thermal barrier coatings. In terms of thermal insulation, due to the high concentration of oxygen vacancies generated inside the lattice when Lu^{3+} replaced Hf^{4+}, its thermal conductivity at 1100 °C was 1.2 W·m^{-1}·K^{-1}, which was about 43% lower than that of the conventional 8YSZ.

Yttrium aluminum garnet

Yttrium aluminum garnet (YAG) is a type of ceramic material with excellent optical, mechanical, thermal and mechanical properties. Fig. 13 shows a schematic diagram of the crystal structure of YAG [106]. YAG

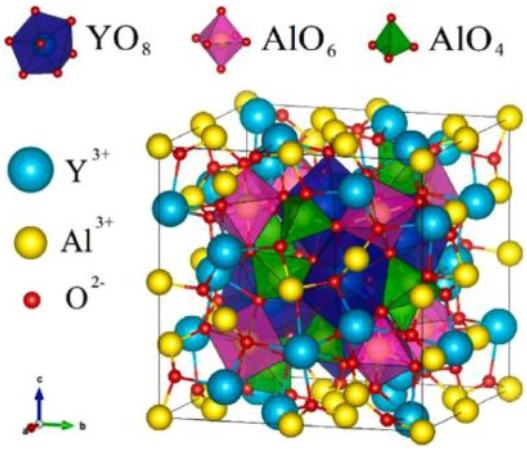

Fig. 13. Crystallographic lattice cell of YAG showing the coordination polyhedra of the cations [106].

belongs to the cubic crystal system crystal structure with the molecular formula $Y_3Al_5O_{12}$, its space group is Oh^{10}-*Ia3d*, and its lattice constant is 1.2002 nm. The number of molecules in the unit cell is 8, with 24 Y^{4+}, 40 Al^{3+}, and 96 O^{2-}, respectively. In the cell structure of YAG, it can be considered as a connected network formed by oxygen tetrahedra, oxygen octahedra and oxygen dodecahedra [107, 108]. O^{2-} is in the dense stacking position, while Y^{4+} and Al^{3+} are in the center of the polyhedra composed of oxygen. In this case, Al^{3+} occupies two different structural positions: The first Al^{3+} occupies the center of the oxygen octahedron surrounded by O^{2-} coordination, with O^{2-} occupying each of the six corners of the octahedron; The second Al^{3+} is located at the center of the oxygen tetrahedron with O^{2-}, and O^{2-} occupying the four corners of the tetrahedron. Y^{4+} is located within the oxygen dodecahedron formed by O^{2-} coordination and constitutes [YO_8].

In the YAG cell structure, the bond length of Y-O is 0.245 nm, and the ionic radii of Y^{3+} and other rare-earth ions are relatively close to each other, which makes it possible to replace the central position of the oxygen dodecahedron by a certain number of other rare-earth ions and optimize the high-temperature performance of YAG ceramics [109].

$Y_3Al_5O_{12}$ is currently the most widely used yttrium aluminum garnet-type ceramic material, which has excellent high-temperature mechanical strength, high-temperature structural stability, and creep resistance. In addition, the oxygen diffusion coefficient of YAG ceramics is much lower than that of conventional YSZ, which proves that it is a type of ceramic material with good high-temperature oxidation resistance and can better protect the bond coat from oxidation [110]. Su et al. [111] prepared a YAG oxygen barrier coat with a thickness of about 10 μm between the YSZ top coat and the bond coat. After heat treatment at 1200 °C for 100 h, the YAG oxygen barrier coat not only suppressed the precipitation of Y_2O_3 from the YSZ, but also drastically

reduced the oxidation rate of the bond coat, and improved the thermal cycle life of the coating. The disadvantage of $Y_3Al_5O_{12}$ is its low coefficient of thermal expansion and high thermal conductivity, which limits its application in high-temperature environments.

To obtain ceramics with low thermal conductivity and high coefficient of thermal expansion, a typical method is to increase the disorder of the structure.

Shuai et al. [112] synthesized a series of $(Y_{1-x}La_x)_3Al_5O_{12}$ ceramics through the chemical co-precipitation method, and investigated the thermophysical properties. The results showed that the doping of La^{3+} significantly improved the Vickers hardness and fracture toughness of the ceramics, the Vickers hardness could reach up to 18.03 GPa, which was 72.5% higher than that of the YAG ceramics; the fracture toughness could reach up to 2.99 $MPa \cdot m^{1/2}$, which was close to that of the traditional YSZ ceramics. In terms of the coefficient of thermal expansion, the doping of La reduced the lattice energy and increased the content of $LaAlO_3$, so that the $(Y_{1-x}La_x)_3Al_5O_{12}$ ceramics exhibited a coefficient of thermal expansion compatible with the YSZ, and the coefficient of thermal expansion of the $(Y_{0.7}La0.3)_3Al_5O_{12}$ ceramics at 1000 °C reaches 9.79×10^{-6} K^{-1}. Xue et al. [113] synthesized a series of $(Y_{1-x}Gd_x)_3Al_5O_{12}$ (x=0, 0.1, 0.2, 0.3, and 0.4) ceramics through chemical co-precipitation route, and investigated the thermophysical properties. The thermal conductivities of the five ceramics are shown in Fig. 14. All the doped ceramics had lower thermal conductivity than the conventional YAG ceramics, and $(Y_{0.8}Gd_{0.2})_3Al_5O_{12}$ had the lowest thermal conductivity, which was only 1.51 $W \cdot m^{-1} \cdot K^{-1}$ at 1200 °C. This was owing to the substitution of Gd^{3+} to enhance the anharmonic interactions within the ceramics and enhanced phonon scattering.

YAG is a potential new type of ceramic material for thermal barrier coatings due to its excellent high-temperature phase stability, good oxidation resistance, and high resistance to sintering. Meanwhile, the excellent optical properties of YAG make it a widely used matrix material in lasers and light-emitting diodes. In the 1980s, researchers developed the Thermal barrier sensor coatings concept [114]. By applying a thermal imaging fluorescent substance to the TBCs and partially modifying the TBCs with photoluminescent rare-earth elements. These new coatings can retain the function of the TBCs, monitoring the internal temperature of the TBCs as well as the thermal gradient between the bond coats and the top coats [115].

Kissel et al. [116] prepared YAG:Eu ceramics and characterized their thermal imaging fluorescence behavior. The results showed that the YAG:Eu ceramics exhibited a very significant temperature-sensitive behavior in the range of 1000-1470 K. In addition, the ambient oxygen concentration had a weak effect on the fluorescence properties of the ceramics, making YAG:Eu more suitable for applications in engine combustion environments. Yu and Omrane et al. [117, 118] prepared YAG:Dy ceramics and characterized their thermal imaging fluorescence behavior. The results showed that the temperature sensitivity of YAG:Dy ceramics was in the range of 300-1773 K up to 1973 K, proving its promising application in the combustion environment of turbine engines. He et al. [119] prepared $Y_3Al_5O_{12}:Ce^{3+}$/8YSZ TBCs by APS, and found that $Y_3Al_5O_{12}:C^{3+}$e and 8YSZ formed alternating and dense microstructures during the deposition process. The results showed that $Y_3Al_5O_{12}:Ce^{3+}$ could improve the high-temperature oxidation resistance of the coatings, and $Y_3Al_5O_{12}:Ce^{3+}$ had good fluorescence luminescence performance, and there was an intrinsic response mechanism between the residual stress inside the ceramic layer and the offset of the peak wavelength of the emission spectrum. When the residual thermal stress inside the ceramic layer increased, the peak wavelength of the emission spectrum shifted to the short-wave direction.

Perovskite oxides

Perovskite oxides have received continuous attention from researchers due to their excellent physicochemical properties. It is considered a potential high-performance

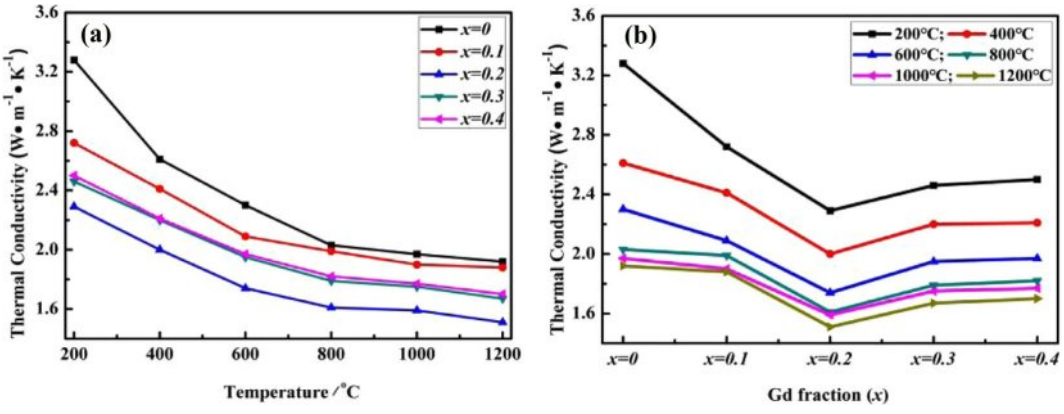

Fig. 14. Thermal conductivities of $(Y_{1-x}Gdx)_3Al_5O_{12}$ (x = 0, 0.1, 0.2, 0.3, and 0.4) bulk samples as a function of temperature (a) and Gd^{3+} doping concentrations (b), respectively [113].

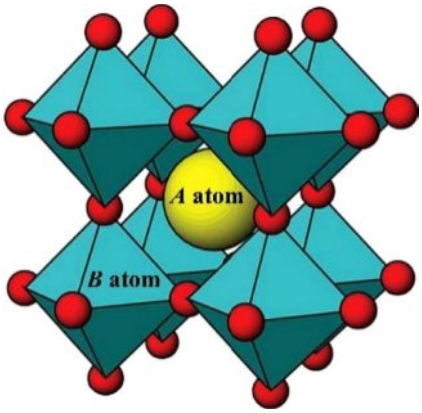

Fig. 15. The ideal cubic perovskite ABO_3 structure [121].

thermal barrier coating material due to its good high-temperature phase stability, moderate mechanical properties, and low thermal conductivity [120]. Fig. 15 shows the crystal structure of ABO_3 cubic perovskite oxides, where the A atoms occupy the center position of the cubic cell, the B atoms occupy the vertex position, and the B-O atoms form a stable [BO_3] octahedral structure [121]. Due to the extensive selectivity of the A and B position ions, the perovskite oxides have tunable chemical bonding and thermodynamic properties. In addition, the A-site and B-site ions can be replaced by cations with different radii and chemical valences, and this solid solution/doping approach can further improve the material properties.

The perovskite zirconates have excellent thermodynamic properties in high-temperature environments and are the most widely investigated perovskite oxide. Among them, SrZrO3 has been proven as one of the most refractory oxides known to science with a melting temperature as high as 2650 °C [122]. With the temperature increasing, $SrZrO_3$ perovskite undergoes three temperature-induced phase transformations, which are as follows [123]:

$$\text{orthorhombic} \xrightarrow{740^{\circ}C} \text{pseudo-tetragonal} \xrightarrow{840^{\circ}C} \text{tetragonal} \xrightarrow{1130^{\circ}C} \text{cubic} \quad (2)$$

As a candidate material for thermal barrier coatings, the phase transformation of $SrZrO_3$ does not have distinguishable discontinuities of the unit cell volumes, and only the transformation from orthorhombic to pseudo-tetragonal involves a small volume change of 0.14%, so the change in temperature does not lead to large stresses within the coating [124]. Liu et al. [125] investigated the thermodynamic properties of several typical perovskite materials by first-principles calculations and explored the relationship between their structures and properties. The results showed that the inhomogeneity of chemical bonding in the ABO_3 (A=Sr, Ba; B=Ti, Zr, and Hf) structure affected the anisotropic thermodynamic properties of perovskite materials.

Liu et al. [126] characterized the properties of $BaZrO_3$ material and found that it had good high-temperature thermodynamic properties. Compared with YSZ, the high-temperature Young's modulus of $BaZrO_3$ at 1473 K was still 81.6% of that at room temperature, and the decay of the modulus was smaller than that of YSZ, which showed better high-temperature resistance. In addition, $BaZrO_3$ had better thermal properties, with a coefficient of thermal expansion of 7.84×10^{-6} K^{-1} and a thermal conductivity of 2.81 $W\cdot m^{-1}\cdot K^{-1}$ at 1473 K. Ma et al. [127] investigated the thermophysical properties of $SrZrO_3$ ceramics and found a phase transformation from orthorhombic to pseudo-tetragonal phases during the thermal expansion coefficient detection. The results showed that the change of crystal structure made the thermal expansion coefficient of $SrZrO_3$ at 1200 °C was more than 4.5% greater than that of conventional YSZ. In addition, the thermal conductivity of $SrZrO_3$ ceramics at 1000 °C was only 2.08 $W\cdot m^{-1}\cdot K^{-1}$, which was lower than that of conventional 8YSZ. Although $SrZrO_3$ ceramics exhibited high coefficients of thermal expansion and low thermal conductivities, it was found that phase transitions and structural destabilization occurred during the heat capacity testing process at elevated temperatures.

To further improve the material properties, obtaining new perovskite-based materials using solid solution/doping has also become a direction of interest for researchers. Liu et al. [128] modified $SrZrO_3$ ceramics using different contents of $La_2Ce_2O_7$ and characterized the thermal conductivity of the four (1-x)$SrZrO_3$-x$La_2Ce_2O_7$ (x=0, 0.3, 0.5, and 1.0) ceramics. The results are shown in Fig. 16. The doping of $La_2Ce_2O_7$ caused mutual ion exchange of Sr^{2+}/Zr^{4+} and La^{3+}/Ce^{4+} inside the ceramics, which increased the content of point defects and local elastic fields inside the ceramics in a high-temperature environment, and decreased the phonons mean free path, so the thermal conductivity of $SrZrO_3$ ceramics decreased with the increase of $La_2Ce_2O_7$ doping content, and it could reach as low as 0.97 $W\cdot m^{-1}\cdot K^{-1}$.

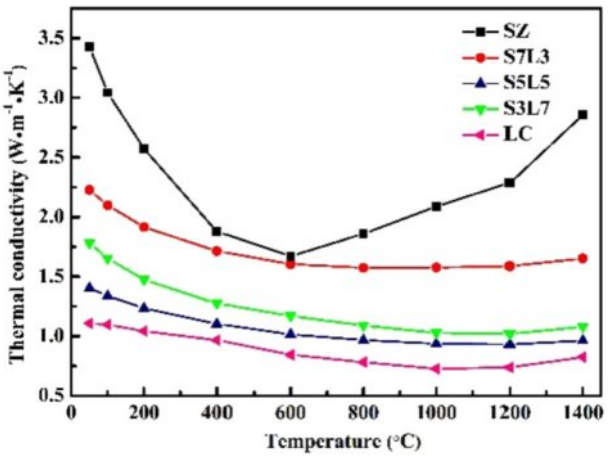

Fig. 16. Thermal conductivities of the (1-x)$SrZrO_3$-x$La_2Ce_2O_7$ (x=0, 0.3, 0.5, and 1) [128].

Zhang et al. [129] prepared $Sr_{0.8}(Zr_{0.9}Yb_{0.05}Gd_{0.05})O_{2.75}$ (SZYG/YGZO) and $Sr(Zr_{0.9}Yb_{0.05}Gd_{0.05})O_{2.95}$ (SZYG) ceramics by the solid-state reaction method and characterized their structural and thermodynamic properties. The results showed that the SZYG/YGZO ceramics, which consisted of SZO and $Yb_{0.5}Zr_{0.5}O_{1.75}$, had a thermal conductivity of about 1.3 $W \cdot m^{-1} \cdot K^{-1}$ at 1000 °C, which was 40% lower than that of SZO ceramics. In addition, the thermal expansion coefficient of SZYG/YGZO ceramics reaches 10.9×10^{-6} K^{-1} at 1250 °C, and the fracture toughness is 30% higher than that of SZO. Yang and Zhang et al. [130, 131] prepared systems $Ca_xSr_{1-x}ZrO_3$ and $Ca_xBa_{1-x}ZrO_3$ perovskite ceramic solid solutions by pressureless sintering and characterized the thermodynamic properties of the two types of ceramics. The results showed that Young's modulus of $Ca_xSr_{1-x}ZrO_3$ (x=0.2, 0.4, 0.6, and 0.8) ceramics at 1200 °C were 157.29 GPa, 152.07 GPa, 147.22 GPa, and 144.82 GPa, which corresponded to the room temperature Young's modulus values of 70.7%, 69.4%, 68.8%, and 71.1%. Young's modulus of $Ca_xBa_{1-x}ZrO_3$ (x=0.05, 0.10, 0.15, 0.20, and 0.25) ceramic solid solution decays at high temperatures by 18.4%, 15.3%, 16.2%, 18.0%, and 20.3%, respectively. However, $SrZrO_3$, $BaZrO_3$, and YSZ ceramics under the same conditions decayed by 35.7%, 18.4%, and 37.1%, respectively, which proved that the two types of solid solution materials exhibited good high-temperature mechanical properties. In terms of the coefficient of thermal expansion, the coefficients of thermal expansion of $Ca_xSr_{1-x}ZrO_3$ and $Ca_xBa_{1-x}ZrO_3$ solid solutions are 10.75-11.23×10^{-6} K^{-1} and 7.7-10.2×10^{-6} K^{-1}, respectively.

Magnetoplumbite compounds

The chemical formula of the Magnetoplumbite compound is $AB_{12}O_{19}$, and usually A is lanthanide elements such as La, Nd, Gd, and Lu; and B is trivalent metal ions such as Al, Gd, and Fe. The $AB_{12}O_{19}$ has a hexagonal crystal structure and belongs to the $P6_3/mmc$ space group. The oxygen ions in its crystal structure are arranged in a hexagonal close-packed, alternately overlapping with $[BO_6]$ octahedra, $[AO_4]$ tetrahedra, and $[BO_4]$ tetrahedra to form the compound $AB_{12}O_{19}$. When the B-site is Al element, it can be denoted as $AO \cdot 6Al_2O_3$, and is referred to as a hexaluminates with magnetoplumbite structure ($AAl_{12}O_{19}$) [132].

To enhance the structural stability, some of the Al^{3+} ions in the crystal structure of $LaAl_{12}O_{19}$ are usually replaced with bivalent or trivalent metal cations to form $LaM_xAl_{11}O_{19}$ compounds. When M is replaced by Mg, $LaMgAl_{11}O_{19}$ (LMA) is formed. Fig. 17 shows the schematic cell structure of LMA, which is composed of $[LaO_{12}]$ tetrahedra containing La^{3+} ions, $(MgAl)O_4$, and AlO_6 [133]. The structural integrity of LMA is mainly because the ordered arrangement of $(MgAl)O_4$ and AlO_6 reduces the voids in the $LaAl_{12}O_{19}$ cell, which enables a perfect combination with the $[LaO_{12}]$ tetrahedra to form a stable, dense crystal structure [134].

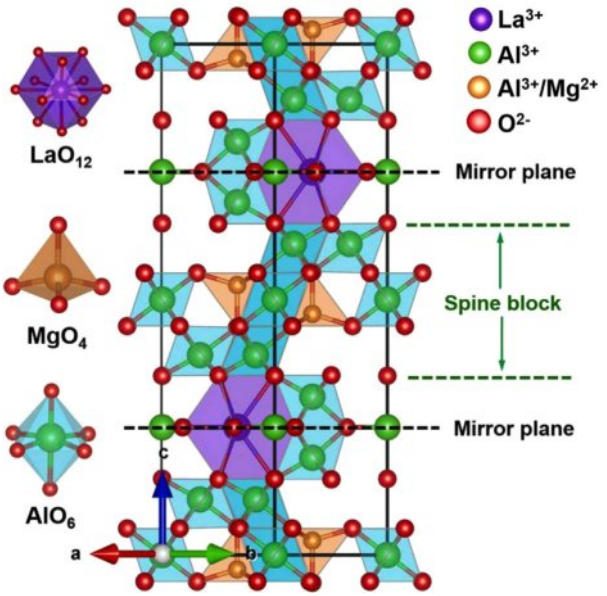

Fig. 17. Schematic crystal structure of $LaMgAl_{11}O_{19}$ [133].

The development of LMA materials has a long history, in the 1980s there was a lot of research on the application of LMA as a matrix for laser components, luminescent materials, and high-temperature catalyst carriers [135-137]. In the last decade, research on LMA in TBCs has been reported, and its special crystal structure gives it unique high-temperature phase stability and excellent electrical insulation properties, making it a potential new ceramic material for the next generation TBCs.

Jiang et al. [138] prepared LMA ceramics by solid-state reaction method and characterized their mechanical as well as thermal properties. The results showed that the flexural strength and fracture toughness of LMA were 353.3±12.5 MPa and 4.60±0.46 $MPa \cdot m^{1/2}$. The Young's Modulus and Possion ratio was 295 GPa and 0.23, respectively. The linear thermal expansion coefficient of $LaMgAl_{11}O_{19}$ ceramic from 200-1200 °C is 9.17×10^{-6} K^{-1}, and thermal conductivity at 1000 °C is 2.55 $W \cdot m^{-1} \cdot K^{-1}$. Sun et al. [139, 140] found that the content of amorphous phase in LMA coatings increased with the increasing of spraying power, which reduced the porosity of the coatings, making the volume shrinkage of the coatings larger and the coefficient of thermal expansion lower. In addition, they investigated the thermal cycling behavior of LMA coatings at 1000 °C. It was found that the spalling of TBCs was mainly related to the formation of TGO and the thermal expansion mismatch between the coating and the substrate. It was confirmed that the lower the amorphous phase content of the LMA coating, the higher the bond strength with the bond coat.

In terms of thermal corrosion behavior, Cui et al. [141] investigated the CMAS corrosion mechanism of LMA coatings. They found that a dissolution-reprecipitation

reaction occurred between LMA and molten CMAS during the corrosion process, and $CaAl_2Si_2O_8$ and $Ca(Mg, Al)(Al, Si)_2O_6$ mixtures were generated in this process. This mixture was highly corrosive at high temperatures, which could seriously corrode the LMA coating and cause cracking and peeling. Tsukada et al. [142] prepared LMA coatings by APS and investigated their corrosion behavior against $Na_2SO_4+V_2O_5$ at 1100 °C. The results showed that the LMA coatings consisted of non-equilibrium amorphous phases, and the amorphous LMA had a significant higher reaction rate with $NaVO_3$, corroded 90% of the coating in almost 30 minutes.

In order to enhance the performance of LMA in ultrahigh-temperature engines, the optimization of LMA primarily relies on the preparation of composite materials and ion doping modification.

In terms of material composites, LMA is mainly used to form composites with YSZ, $(Yb, Er)_2SiO_5$, and $Yb_3Al_5O_{12}$ materials. Chen et al. [143] prepared LMA/YSZ dual ceramic layer thermal barrier coatings (DCL-TBCs) by APS and compared the thermal cycle life with conventional single-layer LMA thermal barrier coatings (SL-TBCs). The results showed that the YSZ intermediate layer could reduce the thermal expansion mismatch between the LMA and the bond coat, and prevented the formation and expansion of cracks. Eventually, the thermal cycle life of DCL-TBCs could reach 6868 cycles, which was higher than that of the conventional SL-TBCs of 6251 cycles. Based on the DCL-TBCs, Chen et al. [144] designed and prepared LMA/YSZ functional gradient TBCs (FG-TBCs). Compared with DCL-TBCs and SL-TBCs, the FG-TBCs exhibited higher strain tolerance and superior thermomechanical properties. The FG-TBCs exhibited a higher coefficient of thermal expansion when the temperature was >1200 °C, which was favorable for suppressing the development of tensile stresses during thermal cycling. In addition, the thermal cycle life of the FG-TBCs at 1350 °C reached 11749 cycles, which was much higher than that of conventional DCL-TBCs (6362 cycles) as well as SL-TBCs (6251 cycles).

Zuo et al. [145] used APS to deposit a novel coating with Er_2SiO_5 as the inner layer and LMA as the top coat on C/SiC composites, and they found that although this coating could improve the high-temperature oxidation resistance of the substrate, the coating was susceptible to liquid sintering, and bubbles were easily generated between the coating and the substrate, which led to coating failure. In addition, Zuo et al. [146] investigated the effect of $Yb_3Al_5O_{12}$ on the performance of LMA materials, and the results showed that $Yb_3Al_5O_{12}$ did not effectively improve the performance of LMA materials, and its thermal conductivity and coefficient of thermal expansion at 1200 °C were 3.9 $W \cdot m^{-1} \cdot K^{-1}$ and 8.41×10^{-6} /K, respectively, unable to meet the performance requirements in the ultrahigh-temperature engine.

In the research of ion doping modification, ion doping or co-doping is mainly performed at the La-site and Al-site of LMA. Currently, the ions for doping substitution at the La-site mainly include Sr^{2+}, Nd^{2+}, Sm^{3+}, Gd^{3+}, Dy^{3+}, and Yb^{3+}; and the doping substitution at the Al-site includes Ti^{2+} and Sc^{3+}. The doping of metal cations produces point defects and high-density grain boundaries in the crystal structure, which can enhance the phonon scattering and reduce the thermal conductivity. Lu et al. [147] optimized the thermophysical properties of LMA material by replacing both La^{3+} and Al^{3+} ions with Nd^{3+} and Sc^{3+} ions, and the results showed that the co-substitution had a significant effect on increasing the coefficient of thermal expansion and decreasing the thermal conductivity. In addition, the thermal conductivity of this material decreased with the increase of the ion doping concentration; the thermal conductivity was as low as 2.04 $W \cdot m^{-1} \cdot K^{-1}$, and the thermal expansion coefficient was as high as 8.53×10^{-6} K^{-1} at 1000 °C. Moreover, the complex doping of Nd^{3+} and Sc^{3+} could also improve the mechanical properties and reduce the material's electrical conductivity. Wang et al. [148] prepared $La_{1-x}Dy_xMgAl_{11}O_{19}$ ceramics with different Dy_2O_3 doping by pressureless sintering and characterized the thermal diffusivities as well as the coefficients of thermal expansion of the different ceramics. The results showed that the thermal diffusivity of $La_{1-x}Dy_xMgAl_{11}O_{19}$ ceramics decreased with the increase of Dy_2O_3 content and reached 2.52-2.89 $W \cdot m^{-1} \cdot K^{-1}$ at 1200 °C. The coefficient of thermal expansion of $La_{0.8}Dy_{0.2}MgAl_{11}O_{19}$ ceramics was higher than those of the undoped LMA ceramics at the same temperature.

At present, the performance of LMA can be effectively improved by ion doping modification. However, there are fewer studies on the modification of LMA materials by Mg-site ion doping. Therefore, in-depth studies on the properties of Mg-site doped LMA series materials are needed. For example, the dopant ion species as well as the ionic ratio should be further regulated to obtain LMA materials with more excellent thermodynamic properties. Explore the reasons for the decrease in thermal conductivity of doped materials and the underlying mechanisms by which factors such as oxygen vacancy defects and ceramic porosity affect the thermodynamic properties of the materials.

High-entropy ceramic

High-entropy ceramics generally refer to solid solutions formed by multiple components in an equiatomic ratio or near equiatomic ratio, without primary or secondary distinction between the components [149]. The concept of high-entropy originated in the field of alloys. Ye et al. [150] first found that high-entropy alloy single-phase solid solutions have typical high-entropy effects. In 2015, Rost et al. [151] reported a high-entropy rare-earth oxide ceramic material with a pyrochlore structure for the first time, and subsequently more and more high-

entropy oxide ceramics with other structures have been synthesized due to the potential of high-entropy ceramics for various applications.

High-entropy effects include [152]: (1) thermodynamics high-entropy effects; (2) structures severe lattice distortion effects; (3) kinetic sluggish diffusion effects; and (4) properties cocktail effects. In recent years, researchers have proposed a variety of new TBCs materials based on the high-entropy effect. Further expanding the research field of new materials by introducing high entropy effect into the modification design of novel TBCs materials. Compensate the performance defects of single-component rare-earth ceramics through the synergistic effect of multiple rare-earth elements [153].

Rare-earth zirconates are one of the most promising TBCs ceramic materials with low thermal conductivity and good high-temperature phase stability. Guo et al. [154] improved the thermal cycle life and fracture toughness of $Gd_2Zr_2O_7$ by optimizing the doping ratio of Sc^{3+} in $Gd_2Zr_2O_7$. Ren et al. [155] reduced the grain size and improved the mechanical properties of TBCs by optimizing the doping ratio of Yb^{3+} in $La_2Zr_2O_7$. In recent years, researchers have developed a variety of high-entropy rare-earth zirconates and have made some progress inspired by high-entropy ceramics.

Li et al. [155] prepared $(La_{0.2}Ce_{0.2}Nd_{0.2}Sm_{0.2}Eu_{0.2})_2Zr_2O_7$ ceramics by flash sintering, the average grain size of the ceramics was 188 nm, and the hardness and fracture toughness reached 6.49±1.25 GPa and 2.16±0.38 $MPa \cdot m^{1/2}$, respectively. Luo et al. [156] successfully synthesized $(La_{0.2}Nd_{0.2}Sm_{0.2}Eu_{0.2}Gd_{0.2})_2Zr_2O_7$ and $(Yb_{0.2}Nd_{0.2}Sm_{0.2}Eu_{0.2}Gd_{0.2})_2Zr_2O_7$ high-entropy pyrochlore ceramics. The two ceramics had good phase stability at 1600 °C. In particular, the $(Yb_{0.2}Nd_{0.2}Sm_{0.2}Eu_{0.2}Gd_{0.2})_2Zr_2O_7$ ceramic had a higher coefficient of thermal expansion (10.52×10^{-6} K^{-1}), a lower thermal conductivity (1.003 $W \cdot m^{-1} \cdot K^{-1}$), and a higher fracture toughness (1.80 $MPa \cdot mm^{1/2}$). Zhao et al. [157] prepared $(La_{0.2}Ce_{0.2}Nd_{0.2}Sm_{0.2}Eu_{0.2})_2Zr_2O_7$ ceramics with a pyrochlore structure using the chemical co-precipitation method. The thermal conductivity of this ceramic was only 0.76 $W \cdot m^{-1} \cdot K^{-1}$, and the average grain size increased from 1.69 μm to 3.92 μm after heat treatment at 1500 °C for 18 hours. In comparison, the average grain size of $La_2Zr_2O_7$ increased from 1.96 μm to 8.89 μm under the same conditions.

Song et al. [158] added non-rare-earth elements when performing high-entropy composition design and prepared six high-entropy ceramics by solid-state reaction method, including $(Ho_{0.25}Y_{0.25}Er_{0.25}Yb_{0.25})_2Zr_2O_7$ and $(Ho_{0.25}Y_{0.25}Er_{0.25}Zn_{0.25})_2Zr_2O_7$. The results showed that the doping of Zn produced a large number of oxygen vacancies and further reduced the thermal conductivity. However, high concentration of Zn^{4+} led to a decrease in the coefficient of thermal expansion, and therefore the Zn^{4+} concentration needed to be optimized to improve the comprehensive performance. Zhang et al. [159] synthesized $(La_{0.2}Gd_{0.2}Y_{0.2}Yb_{0.2}Er_{0.2})_2(Zr_{1-x}Ti_x)_2O_7$ with a single-phase pyrochlore structure using the solid-state reaction method. The average coefficients of thermal expansion ranged from $10.65\text{-}10.84\times10^{-6}$ K^{-1}, and its room-temperature thermal conductivity was significantly lower than that of $La_2Zr_2O_7$. In addition, Ti^{4+} would partially substitute for Zr^{4+}, and the room-temperature thermal conductivity of $(La_{0.2}Gd_{0.2}Y_{0.2}Yb_{0.2}Er_{0.2})_2(Zr_{1-x}Ti_x)_2O_7$ would be significantly decreased with the increase of Ti^{4+} doping content. In particular, when x=0.5, the thermal conductivity at room temperature was only 1.20 $W \cdot m^{-1} \cdot K^{-1}$.

Rare-earth cerium oxides are considered promising ceramic materials for TBCs due to their low thermal conductivity and good phase stability at high temperatures. In recent years, researchers have developed high-entropy rare-earth cerium oxides by compositional design of the Re-site in $Re_2Ce_2O_7$. Ping et al. [160] Prepared the $(La_{0.2}Nd_{0.2}Sm_{0.2}Gd_{0.2}Dy_{0.2})_2Ce_2O_7$, $(La_{0.2}Nd_{0.2}Sm_{0.2}Gd_{0.2}Yb_{0.2})_2Ce_2O_7$, and three other high-entropy ceramics by sol-gel method and heat-treated the ceramic blocks at 1600 °C for 10 h. The results showed that all the high-entropy ceramics had a single fluorite structure and uniform elemental distribution, and the grain growth rate at 1500 °C was significantly less than that of $Nd_2Ce_2O_7$, with a thermal conductivity lower than 8YSZ and a coefficient of thermal expansion higher than 8YSZ. Xu et al. [161] synthesized $(La_{0.2}Nd_{0.2}Gd_{0.2}Er_{0.2}Yb_{0.2})_2Ce_2O_7$, $(La_{0.2}Nd_{0.2}Sm_{0.2}Gd_{0.2}Y_{0.2})_2Ce_2O_7$, and four other high-entropy ceramics by solid-state reaction method and characterized their properties. The results showed that the coefficient of thermal expansion of the high-entropy ceramics reached $11.92\text{-}12.11\times10^{-6}$ K^{-1}, and the thermal conductivities were 1.52-1.55 $W \cdot m^{-1} \cdot K^{-1}$. In addition, the coefficient of thermal expansion of high-entropy $Re_2Ce_2O_7$ could be regulated by designing the average radius of the cation at Re-site, which was favorable for a better bond behavior of the ceramic coatings with the metal substrate. Zhang et al. [162] synthesized $(La_{0.25}Nd_{0.25}Yb_{0.25}Y_{0.25})_2Ce_2O_7$ and $(La_{0.25}Dy_{0.25}Yb_{0.25}Y_{0.25})_2Ce_2O_7$ high-entropy ceramics with a single fluorite structure by sol-gel method. The results showed that the thermal conductivities of both ceramics were lower than 7YSZ, and the coefficients of thermal expansion were higher than 7YSZ. Because the ionic radius of Nd was larger than that of Dy, the $(La_{0.25}Nd_{0.25}Yb_{0.25}Y_{0.25})_2Ce_2O_7$ ceramic had a higher coefficient of thermal expansion. On this basis, they also prepared $(La_{1/6}Nd_{1/6}Yb_{1/6}Y_{1/6}Sm_{1/6}Lu_{1/6})_2Ce_2O_7$ ceramics by sol-gel method, which also had excellent thermal insulation properties as well as higher thermal expansion coefficients [163].

At present, most of the studies on high-entropy ceramics for TBCs are mainly conducted by analyzing ceramic green bodies, and they are not applied to the preparation of actual coatings. The research on whether

the coating preparation methods will lead to the bias polymerization and volatilization of the elements inside the solid solution of high-entropy ceramics, and whether the coating microstructure will weaken the coating properties have not been sufficiently carried out. The future application of high-entropy ceramics in thermal barrier coatings should not be limited to the composition design of high-entropy ceramics. Research on the optimization of the powder synthesis process, the design of ceramic materials with specific properties according to environmental needs, and the synthesis of high-purity ceramic materials with controlled powder sizes should also be fully carried out.

Rare-earth tantalates

Rare-earth tantalates are considered as new TBC materials with great potential to replace conventional YSZ. Rare-earth tantalates have good fracture toughness in high-temperature environments due to their ferroelastic toughening mechanism [164]. There are three main types of rare-earth tantalates that have been extensively researched, including $ReTaO_4$, Re_3TaO_7, and $ReTa_3O_9$ [165].

$ReTaO_4$

The research on $ReTaO_4$ has been mainly focused on the optical aspect, which has excellent optical properties, chemical stability, and thermal stability [166]. The research on $ReTaO_4$ in the field of thermal barrier coatings has been developed only recently. Yokogawa et al. [167] investigated the melting points of almost all rare-earth tantalates with $ReTaO_4$ structures, and the results showed that the melting points of $ReTaO_4$-type rare-earth tantalates were all higher than 2000 °C, which meet the high-temperature service conditions for thermal barrier coatings. Feng and Shian et al. [164, 168] investigated the phase transformation behavior of $YTaO_4$ at high-temperatures by first principles and experiments. The results showed that $YTaO_4$ was a monoclinic phase at room temperature, when the temperature reached 1426±7 °C, $YTaO_4$ would be transformed from monoclinic phase to tetragonal phase. Compared with the phase transition behavior of YSZ, the phase transformation of $YTaO_4$ was a ferroelastic phase transformation, and there was no obvious volume change. The crystal structure of ferroelastic m-$ReTaO_4$ ceramics at room temperature is shown in Fig. 18 [169]. The rare-earth and tantalum atoms have different periodicities and are located in different atomic planes. The rare-earth atoms are coordinated with eight oxygen atoms to form [ReO_8] polyhedra, which is similar to the case of the metastable monoclinic phase structure. Tantalum atoms coordinate with four oxygen atoms to form twisted [TaO_4] tetrahedra, and the individual [TaO_4] tetrahedra are independent of each other in the lattice and not directly connected, which is conducive to increasing the mobility of the atoms in high-temperature environments and facilitating the ferroelastic phase transformation. The crystal structure of t-$YTaO_4$ at high-temperature environment is also shown in Fig. 18 [169]. The rare earth and tantalum atoms are located in the same atomic plane with the same periodicity, while the tantalum atoms are coordinated with four oxygen atoms to form regular [TaO_4] tetrahedra. The degree of distortion is less than that of $ReTaO_4$ ceramics with monoclinic and metastable monoclinic phases. Wang et al. [170, 171] compared some of the $ReTaO_4$ (Re=Y, Er, Lu, Yb, Nd, Eu, and Gd) with YSZ in terms of thermal conductivity. The results showed that almost all $ReTaO_4$ had lower thermal conductivity, which was reduced 8-40% compared with conventional YSZ. Zhou et al. [172] investigated the effect of HfO_2 doping content on the properties of $SmTaO_4$, and the thermal conductivity of $SmTaO_4$ was significantly reduced when the doping amount was 10 mol.%. Based on the above findings, the researchers improved the performance of $ReTaO_4$ further by elemental doping.

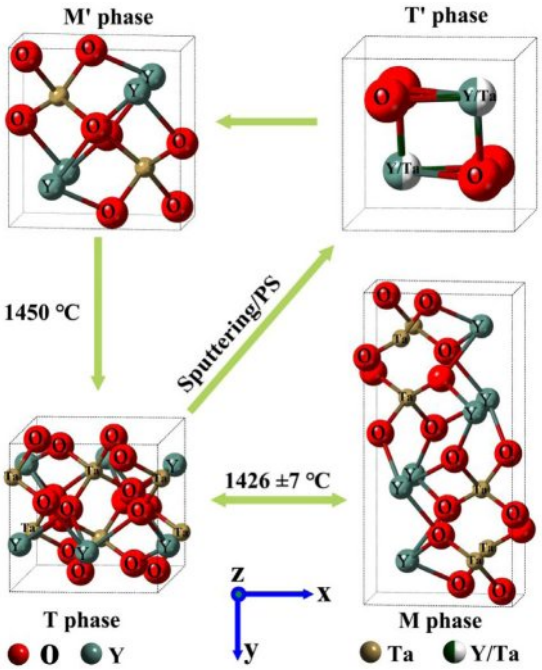

Fig. 18. Schematic diagram of the structural transformation of $YTaO_4$ [169].

Wu et al. [173] found that using Al^{3+} ions to dope $DyTaO_4$ could effectively improve the high-temperature toughness of the material. In addition, due to the difference in ionic radius and atomic mass between Al^{3+} and rare-earth elements, a large number of defects could be introduced by Al^{3+} doping, which disturbed the orderliness of the matrix lattice and increased the phonon scattering. Thus, the thermal conductivity of $(Al_xDy_{1-x})TaO_4$ ceramics decreased with the increase of Al^{3+} doping content. Wang et al. [174] prepared $(Y_{0.2}Ce_{0.2}Sm_{0.2}Gd_{0.2}Dy_{0.2})TaO_4$ ($5Re_{0.2}TaO_4$) high-entropy

rare-earth tantalates and verified the properties by first-principle calculations. The results showed that the thermal conductivity of $5Re_{0.2}TaO_4$ ceramics was only 1.2-2.6 $W \cdot m^{-1} \cdot K^{-1}$, which was lower than that of the single-component $ReTaO_4$ and YSZ, and the coefficient of thermal expansion reached 10.3×10^{-6} K^{-1} at 1200 °C. In addition, the $5Re_{0.2}TaO_4$ ceramics possessed higher fracture toughness and lower brittleness index, and the low Young's modulus was beneficial for improving the strain tolerance of the coatings. Zhu et al. [175] synthesized high-entropy rare-earth tantalates $(Nd_{1/4}Sm_{1/4}Eu_{1/4}Gd_{1/4})TaO_4$, $(Nd_{1/5}Sm_{1/5}Eu_{1/5}Gd_{1/5}Dy_{1/5})TaO_4$, and $(Nd_{1/6}Sm_{1/6}Eu_{1/6}Gd_{1/6}Dy_{1/6}Ho_{1/6})TaO_4$ by solid-state reaction method. The three ceramics were single-phase solid solutions with a monoclinic structure and a uniform distribution of rare-earth elements, which exhibited excellent high-temperature phase stability at 1200 °C. In terms of thermodynamic behavior, all the ceramics exhibited low thermal conductivity (2.98-1.23 $W \cdot m^{-1} \cdot K^{-1}$, 100-1000 °C), and the coefficient of thermal expansion and fracture toughness of $(Nd_{1/6}Sm_{1/6}Eu_{1/6}Gd_{1/6}Dy_{1/6}Ho_{1/6})TaO_4$ reached 9.25×10^{-6} K^{-1} and 9.97±2.2 GPa, respectively.

Re_3TaO_7

The Re_3TaO_7 system has many excellent properties, including demagnetization, photocatalytic properties, and dielectric properties [176, 177]. These properties are mainly attributed to its own intrinsic structure. The crystal structure of Re_3TaO_7 is shown in Fig. 19 [178]. In the Re_3TaO_7 cell, four tetravalent metal ions are replaced by three trivalent ions (Re^{3+}) and one pentavalent ion (Ta^{5+}), and an oxygen vacancy is created. The oxygen vacancy is a special lattice defect, which can significantly enhance phonon scattering, resulting in a decrease in the phonon mean free path of Re_3TaO_7 and decrease the thermal conductivity.

Due to the complex structure of Re_3TaO_7 ceramics for high-temperature applications, the development of mechanical and thermophysical properties of Re_3TaO_7 ceramics will be a new trend in the application of thermal barrier coatings [179]. Chen et al. [180] prepared a variety of Re_3TaO_7 (Re=La, Nd, Sm, Eu, Gd, and Dy) ceramics by solid-state method and characterized their properties. The results showed that the thermal conductivity of Re_3TaO_7 ceramics is 1.1-2.1 $W \cdot m^{-1} \cdot K^{-1}$, which was much lower than that of conventional YSZ. Moreover, their thermal conductivity showed a tendency to decrease with the increase of temperature. The thermal conductivity of Re_3TaO_7 (Re=La, Nd) showed a slight increase in the high temperature environment, and this phenomenon could be attributed to the influence of thermal radiation effect. In terms of thermal expansion behavior, the coefficients of thermal expansion of the Re_3TaO_7 ceramics increased with temperature and the maximum value was close to 8YSZ, except for Sm_3TaO_7, which showed negative expansion due to a phase transformation.

In the research of Re_3TaO_7 doping modification, Chen et al. [181] successfully doped ZrO_2 into Eu_3TaO_7 ceramics, and it was found that due to the replacement of Ta^{5+} and Eu^{3+} by Zr^{4+} (Fig. 20), which resulted in the radius and atomic mass differences between the ions, the thermal conductivity of the ceramics was decreased with the increase of ZrO_2 content (1.37 $W \cdot m^{-1} \cdot K^{-1}$, 900 °C). In addition, the alloying effect of ZrO_2 weakened the lattice energy, which increased the coefficient of thermal expansion of Eu_3TaO_7 (10.7×10^{-6} K^{-1}, 1100 °C).

Sang et al. [182] prepared $(Sm_{0.2}Gd_{0.2}Dy_{0.2}Y_{0.2}Yb_{0.2})_3TaO_7$ ($5Re_3TaO_7$) ceramics by solid-state reaction method and characterized their crystal structure, microstructure, elemental distribution, structural stability and thermophysical properties. The results showed that the $5Re_3TaO_7$ had a single defective fluorite structure, uniform element

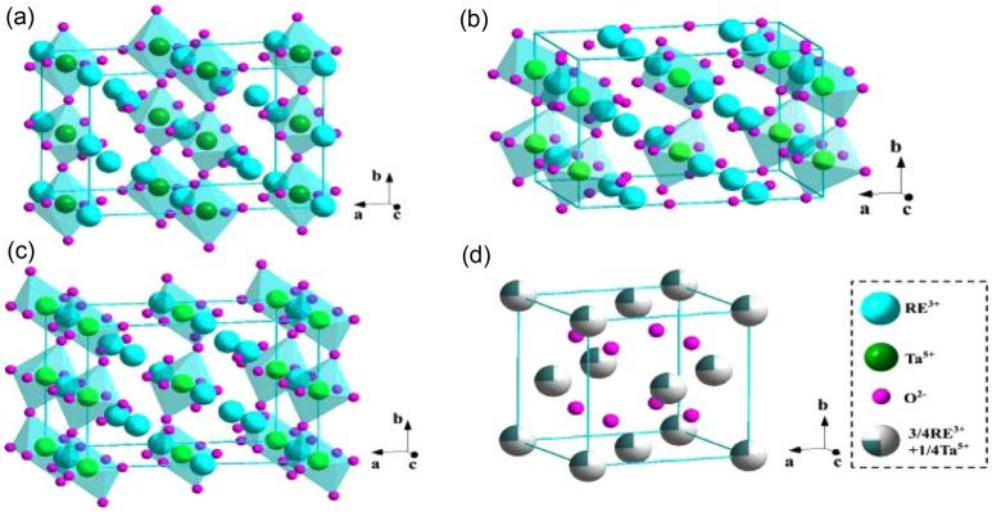

Fig. 19. Crystal structures of RE_3TaO_7 (RE = rare earth) ceramics with different space group: (a) Cmcm, (b) C2221, (c) Ccmm, (d) Fm-3m [178].

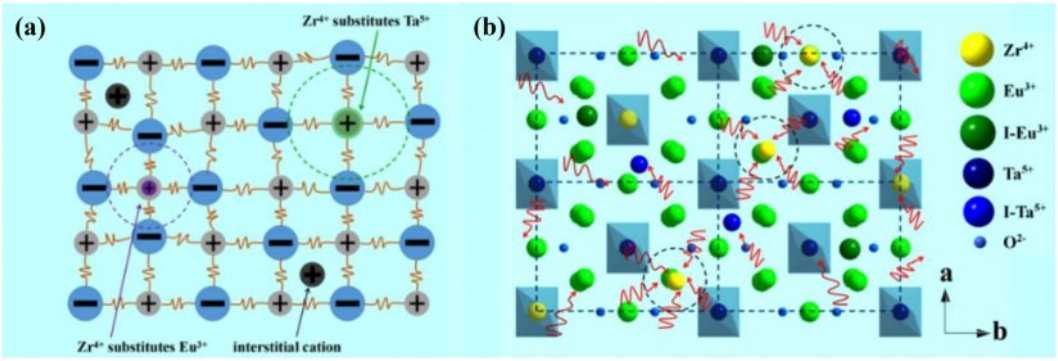

Fig. 20. Schematic drawings of x mol% ZrO_2-Eu_3TaO_7 (x = 0, 3, 6, 9, 12, 15) ceramics: (a) Zr^{4+} ions substitute Ta^{5+} and Eu^{3+} ions, (b) crystal structure and principle diagram of phonon scattering in 2×2×1 supercell of ZrO_2 alloying Eu_3TaO_7 ceramics, I-Eu^{3+} and I-Ta^{5+} represent the interstitial Eu^{3+} and Ta^{5+} ions, respectively [181].

distribution, and grain size between 0.2-3 μm. After high-temperature cyclic heat treatment, the single fluorite structure was maintained, which showed good high-temperature structural stability. In addition, the thermal conductivity of $5Re_3TaO_7$ was 0.72-0.74 $W \cdot m^{-1} \cdot K^{-1}$ in the range of 25-800 °C, which was much lower than that of 7YSZ, and the coefficient of thermal expansion at 1200 °C was about 5.6×10^{-6} K^{-1}, which was lower than that of the requirements of the surface ceramic coat materials for TBCs.

$ReTa_3O_9$

The crystal structure of $ReTa_3O_9$-type rare-earth tantalates is similar to that of perovskite-type materials, and is referred to as a defective perovskite structure [183]. $ReTa_3O_9$ is considered as one of the candidates for TBCs due to its large relative molecular mass and complex crystal structure.

Chen et al. [184] successfully prepared $ReTa_3O_9$ (Re=Ce, Nd, Sm, Eu, Gd, Dy, and Er) ceramics by solid-state method. The microstructures are shown in Fig. 21. All ceramics had uniformly sized grains, well-defined grain boundaries, and a small number of pores. The presence of pores was favorable to improve the scattering of phonons as well as the reduction of thermal conductivity. Fig. 22 exhibits the thermophysical properties of $RETa_3O_9$, with the lowest value of thermal conductivity up to 1.3 $W \cdot m^{-1} \cdot K^{-1}$ (900 °C), since phonons could be effectively scattered by the complex crystal structure, lattice defects, and grain boundary. It should be emphasized that the thermal conductivity of $ReTa_3O_9$ increased with temperature due to the presence of distorted [TaO_6] octahedra and a high concentration of cationic vacancies in $ReTa_3O_9$. Moreover, the coefficient of thermal expansion and fracture toughness of $ReTa_3O_9$ made it unsuitable for TBCs.

To improve the application prospects of $ReTa_3O_9$, researchers have improved its usability through high-entropy design. Chen et al. [185] prepared $(La_{1/5}Pr_{1/5}Dy_{1/5}Ho_{1/5}Tm_{1/5})Ta_3O_9$, $(Gd_{1/5}Dy_{1/5}Ho_{1/5}Er_{1/5}Tm_{1/5})Ta_3O_9$, $(La_{1/6}Sm_{1/6}Eu_{1/6}Dy_{1/6}Ho_{1/6}Tm_{1/6})Ta_3O_9$, and $(Eu_{1/6}Gd_{1/6}Dy_{1/6}Ho_{1/6}Er_{1/6}Tm_{1/6})Ta_3O_9$ by spark plasma sintering. The results showed that all the ceramics had a single perovskite structure, and had low thermal conductivity (1.50 $W \cdot m^{-1} \cdot K^{-1}$), high hardness (10 GPa), appropriate Young's modulus (180 GPa), and high fracture toughness (2.5 $MPa \cdot m^{1/2}$).

Liu et al. [186] prepared YTa_3O_9 ceramics by solid-state reaction method and characterized their high-temperature phase transformation behavior, the results showed that the synthesized YTa_3O_9 ceramics would transform from orthorhombic to tetragonal phase at 300-400 °C.

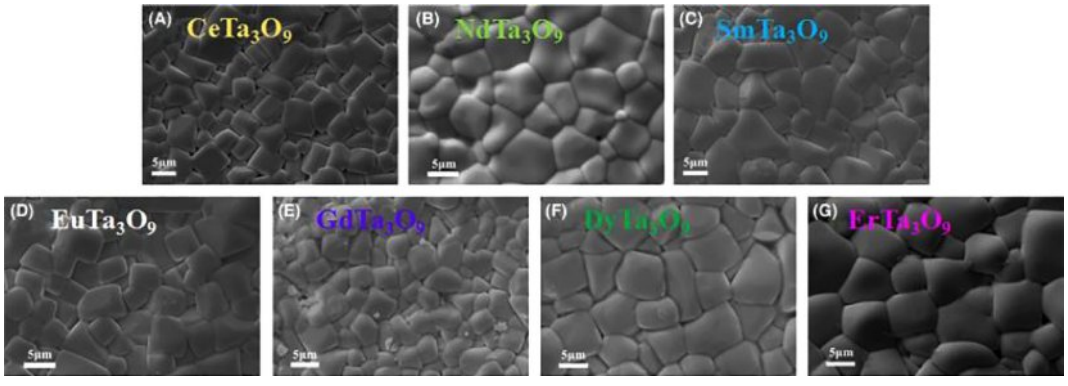

Fig. 21. Typical microstructure of $ReTa_3O_9$ (RE = Ce, Nd, Sm, Eu, Gd, Dy, Er) ceramics [184].

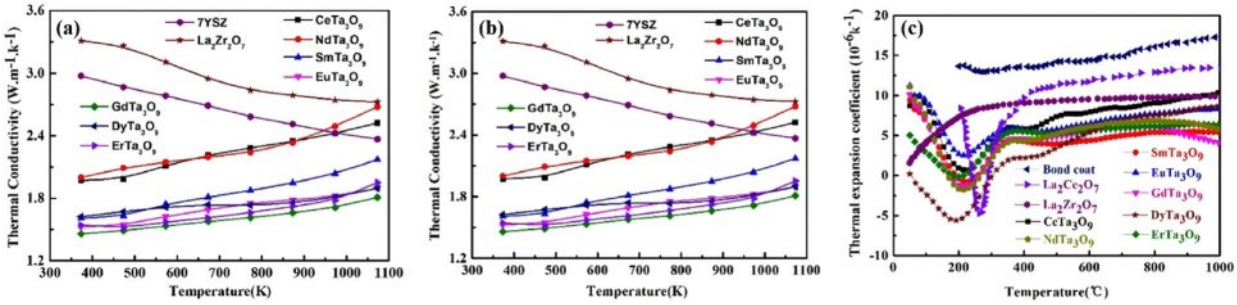

Fig. 22. (a) Thermal conductivity for $ReTa_3O_9$ samples, (b) The comparison of the thermal conductivity of the 7YSZ, $La_2Zr_2O_7$, and experimental $ReTa_3O_9$, (c) CTEs comparison among $ReTa_3O_9$ compounds and other TBCs [184].

To suppress this phase transformation behavior, they designed and synthesized $(Y_{0.2}La_{0.2}Ce_{0.2}Nd_{0.2}Gd_{0.2})Ta_3O_9$ ceramics with a tetragonal structure. High-temperature XRD analysis showed that the high-entropy effect effectively inhibited the phase transformation. Meanwhile, the thermal conductivity of $(Y_{0.2}La_{0.2}Ce_{0.2}Nd_{0.2}Gd_{0.2})Ta_3O_9$ at 1100 °C was only 1.69 $W{\cdot}m^{-1}{\cdot}K^{-1}$, which was about 11% lower compared with YTa_3O_9. In addition, the $(Y_{0.2}La_{0.2}Ce_{0.2}Nd_{0.2}Gd_{0.2})Ta_3O_9$ had high fracture toughness (3.57 $MPa{\cdot}m^{1/2}$) as well as good high-temperature thermal stability. However, the coefficient of thermal expansion of $(Y_{0.2}La_{0.2}Ce_{0.2}Nd_{0.2}Gd_{0.2})Ta_3O_9$ at 1500 K was only 6.84×10^{-6} K^{-1}, so it was necessary to consider a multilayer structure or a functional gradient structure in practical applications.

In summary, rare-earth tantalates have lower thermal conductivity, lower Young's modulus, and higher fracture toughness. In addition, rare-earth tantalate is an oxygen ion transport insulator, which can effectively prevent the growth of TGO and extend the thermal cycle life of TBCs. The structure and properties can be further optimized by modifying the rare-earth tantalate. Currently, the researches on rare-earth tantalate ceramics mainly focus on the preparation of ceramic blocks, organizational structure, and thermophysical properties. However, in the process of TBCs preparation, the differences in composition, structure, and preparation methods will have an impact on the performance of the coating. Therefore, the preparation of rare-earth tantalate thermal barrier coatings and the optimization of preparation parameters are the focus of future research. In addition, the ablation resistance, thermal shock resistance, and sintering resistance of the coatings are also significant for their service life and need to be systematically investigated.

Rare-earth niobates

Rare-earth niobates have similar crystal structures to rare-earth tantalates, also having the $ReNbO_4$, Re_3NbO_7, $ReNb_3O_9$, and $Re_2Nb_{15}O_{33}$ systems [187-189]. $ReNb_3O_9$ and $Re_2Nb_{15}O_{33}$ will not be used for TBCs due to their low melting points. Therefore, the RE_3NbO_7 and $RENbO_4$ with relatively high melting points may be suitable for TBCs materials [190]. The disordered distribution of oxygen vacancies and the large chemical inhomogeneity in the structures of the three rare-earth niobates lead to a low thermal conductivity and a low-temperature dependence of the thermal conductivity.

Chen et al. [191] characterized the thermodynamic properties of $ReNbO_7$ (Re=La, Nd, Sm, Eu, Gd, and Dy) ceramics, and the thermal conductivity of the four ceramics was as low as 1.0 $W{\cdot}m^{-1}{\cdot}K^{-1}$ due to the higher content of oxygen vacancies and lattice distortions within the crystals. In recent years, research on rare-earth niobate thermal barrier coatings mainly consists of two aspects: (1) Improve the thermomechanical properties of ceramics by introducing rare-earth cations; (2) Investigate the properties of rare-earth niobates with non-standard stoichiometric ratios and optimize the coating properties by changing the elemental composition.

In the direction of rare-earth cation doping, Zhu et al. [192] prepared $(Dy_{0.25}Er_{0.25}Y_{0.25}Yb_{0.25})_3NbO_7$ ($4Re_3NbO_7$) and $(Dy_{0.2}Ho_{0.2}Er_{0.2}Y_{0.2}Yb_{0.2})_3NbO_7$ ($5Re_3NbO_7$) by solid-state method. The results showed that the thermal conductivities of the two materials were only 0.862 $W{\cdot}m^{-1}{\cdot}K^{-1}$ and 0.724 $W{\cdot}m^{-1}{\cdot}K^{-1}$ at room temperature, and the thermal conductivity of $5Re_3NbO_7$ was lower than that of $4Re_3NbO_7$, one-component niobate, and YSZ at room temperature. In addition, the coefficients of thermal expansion of $5Re_3NbO_7$ and $4Re_3NbO_7$ at 1200 °C are 10.2×10^{-6} K^{-1} and 9.7×10^{-6} K^{-1}, respectively.

In terms of elemental composition, there is more extensive research on non-standard stoichiometric ratio gadolinium zirconate thermal barrier coatings, while less research has been done on rare-earth niobates in this aspect. Huang et al. [193] analyzed the structure and properties of non-standard stoichiometric ratio $Y_{1-x}Nb_xO_{1.5+x}$ coatings, and found that an abnormal increased in the cationic conductivity of the coatings occurs when the ratio of Y/Nb varies around 3:1. In addition, the elastic modulus of the coating increased with the increase of Nb content, but the Vickers hardness as well as the fracture toughness did not show any significant change due to the inefficient effect of the changes in grain size and porosity, and the Y_3NbO_7 was found to have the lowest

thermal conductivity, the best mechanical properties, and the slowest sintering rate after comparison.

Rare-earth silicates

In recent years, with the continuous development of the aerospace industry, the research and development of a new generation of high thrust-to-weight ratio aero-engines is imminent. SiC_f/SiC ceramic matrix composites (CMC) are considered to be ideal materials for aero-engine hot-end components due to their high bearing temperature (1450 °C), low density (2.8 g/cm^2), and excellent high-temperature mechanical properties, and have been successfully applied to hot-end components such as combustion chambers, turbine outer rings, and turbine guide vanes [194, 195]. It has been proven that the use of CMC instead of high-temperature alloys can reduce the mass of engine structural components by 50-70%, reduce cooling air by 20-50%, and substantially improve engine fuel efficiency [196].

The main shortcoming of CMC for large-scale application in aero-engine hot-end components is its weak durability in high-temperature water-oxygen environments [197]. In a dry atmosphere above 800 °C, the surface of CMC can oxidize to generate a dense SiO_2 protective layer [198]. Due to the low diffusion rate of O_2 in SiO_2, CMC has excellent resistance to high-temperature oxidation in dry environments. However, in the service environment of aerospace engines fueled by aviation kerosene, water vapor from combustion reacts with SiO_2 to form volatile $Si(OH)_4$. $Si(OH)_4$ is repeatedly flushed by high-speed gas streams, resulting in continuous exposure of CMCs to gas, which accelerates the process of CMCs depletion and ultimately triggers a drastic deterioration of the mechanical properties [199]. To break through the shortcomings of CMC's high-temperature water-oxygen corrosion resistance, the preparation of environmental barrier coatings (EBCs) on the surface of CMC is the most effective solution [200].

Rare-earth silicates have become the most promising candidate for EBCs due to their low coefficient of thermal expansion, high temperature thermo-chemical stability, and excellent resistance to water and oxygen corrosion [201]. Rare earth silicates are very diverse and have a variety of crystal structures. From the chemical formula, rare-earth silicates can be divided into rare-earth monosilicate (Re_2SiO_5) and rare-earth disilicates ($Re_2Si_2O_7$) [202].

Re_2SiO_5

The ratio of Re_2O_3 and SiO_2 in Re_2SiO_5 is 1:1. When the rare-earth ion radius is large (Re=La, Ce, Pr, Nd, Sm, Eu, and Gd), it will form X1-Re_2SiO_5 with the space group $P2_1/C$ (Fig. 23(a)); When the rare-earth ion radius is small (Re=Tb, Dy, Ho, Er, Tm, Yb, and Lu), it will form X2-Re_2SiO_5 with the space group $C2/c$ (Fig. 23(b)) [203, 204]. The transition temperatures of the two structures are 1190 °C, when Re = Y or Yb, both structures can be formed to exist at the same time. Both X1-Re_2SiO_5 and X2-Re_2SiO_5 can be viewed as consisting of ReO_x (X=6, 7, 8 and 9) polyhedra and SiO_4 tetrahedra, with the difference between the two structures is the number of rare-earth atom coordination: The two rare-earth atom positions in X1-Re_2SiO_5 are 7-coordinated and 9-coordinated to oxygen, forming [ReO_7] and [ReO_9] polyhedra, respectively; The two rare-earth atom positions in X2-Re_2SiO_5 are 6-coordinated and 7-coordinated to oxygen, forming [ReO_6] and [ReO_7] polyhedra, respectively [205].

Among the rare-earth monosilicates, X1-Re_2SiO_5 is more difficult to prepare and has poor high-temperature phase stability, so the research mainly focuses on the luminescent properties of rare-earth doped materials. Compared with X1-Re_2SiO_5, X2-Re_2SiO_5 ceramics have relatively small coefficient of thermal expansion and low thermal conductivity, which are more suitable for environmental barrier coating materials. Li et al. [206] calculated and compared the lattice vibration and thermal conductivity behavior of X2-Re_2SiO_5 (Re=Dy, Ho, Er, Tm, Lu, and Yb) materials by first principles. The results showed that these materials had low thermal conductivity, and the thermal conductivity increased with the increase of rare earth atomic number. Tian et al. [204] tested the thermodynamic properties of X2-Re_2SiO_5 (Re=Tb, Dy, Ho, Er, Tm, Lu, Y, and Yb). The results showed that these materials had excellent high-temperature stiffness and low thermal conductivity. In particular, the thermal conductivity, bending strength

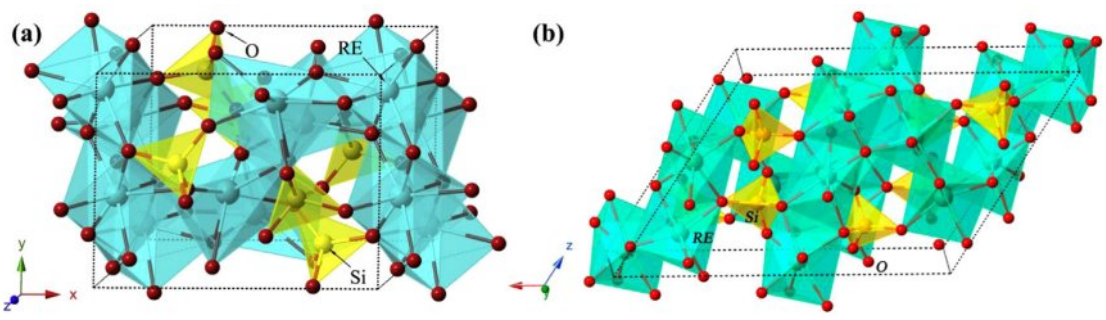

Fig. 23. (a) Crystal structure of X1-RE_2SiO_5, (b) Crystal structure of X2-RE_2SiO_5 [203, 204].

and thermal shock resistance were closely related to the rare-earth species, while the modulus of elasticity and coefficient of thermal expansion were insensitive to the rare-earth element species.

Due to the low thermal conductivity, good phase stability, and excellent resistance to water vapor and CMAS corrosion, the conventional RE_2SiO_5 is a candidate material for EBCs with great performance advantages. However, the coefficient of thermal expansion of Re_2SiO_5 is 6.94-8.84×10^{-6} K^{-1}, which is significantly higher than that of SiC_f/SiC composites (3.5-5.5×10^{-6} K^{-1}) [207]. To apply RE_2SiO_5 to EBCs practically, it is necessary to reduce their coefficients of thermal expansion to achieve good thermal matching.

Ren et al. [208] prepared single-phase X2-$(Y_{0.25}Ho_{0.25}Er_{0.25}Yb_{0.25})_2SiO_5$ ($4ReSiO_5$) high-entropy ceramics and characterized their thermal properties. The results showed that the component effect played an important role in reducing the coefficient of thermal expansion of the high-entropy ceramics compared to the single Re_2SiO_5 (Re=Y, Ho, Er, and Yb), and the coefficient of thermal expansion of $4Re_2SiO_5$ was only 6.82×10^{-6} K^{-1} at 1200 °C. In addition, the room-temperature thermal conductivity of the $4Re_2SiO_5$ was reduced by 5.4-66.8% compared to those of the four single-component Re_2SiO_5. The synergistic reduction of the coefficient of thermal expansion and the thermal conductivity resulted in a better matching behavior between the high-entropy ceramics and CMCs, which effectively reduced the internal stresses of EBCs while providing better thermal insulation.

Ridley et al. [209] prepared $(Sc_{0.2}Y_{0.2}Dy_{0.2}Er_{0.2}Yb_{0.2})_2SiO_5$ high-entropy ceramics by spark plasma sintering and compared the anisotropy of the CTE with Re_2SiO_5 (Re=Sc, Y, Nd, Dy, Er, and Yb) ceramics. The results showed that all the rare-earth monosilicates have very obvious anisotropy of the CTE, with the a-axis CTE lower than 3.64×10^{-6} K^{-1} from room temperature to 1200 °C, while the corresponding CTE in the c-axis direction are usually 9-10×10^{-6} K^{-1}. Chen et al. [210] prepared $(Yb_{0.25}Y_{0.25}Lu_{0.25}Er_{0.25})_2SiO_5$ ($4Re_2SiO_5$) high-entropy ceramics by solid-state reaction method and investigated the thermal expansion behavior of the material from room temperature to 1200 °C using X-ray diffraction (XRD) and crystal-structure refinement methods. The results showed that the CTE of the $4Re_2SiO_5$ exhibited significant anisotropy: α_a=(2.57±0.07)×10^{-6} K^{-1}, α_b=(8.07±0.13)×10^{-6} K^{-1}, α_c=(9.98±0.10)×10^{-6} K^{-1}. Based on the above study, Chen et al. [211] further proposed to utilize the anisotropy of thermal expansion to match the CTE of the coating with that of the metal/ceramic substrate by controlling the crystal orientation of the rare-earth monosilicate coatings purposefully.

$Re_2Si_2O_7$

The ratio of Re_2O_3 to SiO_2 in $Re_2Si_2O_7$ is 1:2. There are seven crystalline forms of $Re_2Si_2O_7$ depending on the rare-earth ionic radii and sintering temperatures, including: A, B (α), C (β), D (γ), E (δ), F, and G. All crystal forms can be viewed as consisting of ReO_x (x=6, 7, and 8) polyhedra with SiO_4 tetrahedra [212].

Table 2 shows the structure of the different crystals and the associated features, respectively [213]. It can be seen that the complex crystal structure and low symmetry of $Re_2Si_2O_7$ contribute to their low thermal conductivity. It is important to note that there is no information about $Y_2Si_2O_7$ ceramics listed in Table 2. This is because $Y_2Si_2O_7$ has seven crystal structures, which form different phases at different temperature ranges. The following phase transitions exist between α, β, γ, and δ [213]:

$$\alpha \xrightarrow{1250\pm10^{\circ}C} \beta \xrightarrow{1445\pm10^{\circ}C} \gamma \xrightarrow{1535\pm10^{\circ}C} \delta \quad (3)$$

Due to the narrow phase region of $Y_2Si_2O_7$, it is challenging to synthesize single-phase $Y_2Si_2O_7$ since the formation temperatures between different structural crystalline forms are relatively close. In addition, phase transformation leads to the formation of cracks within the coating, so the EBC materials have strict requirements for phase stability. Limited by the polymorphic phase transition of rare-earth disilicates, only a few materials, such as β-$Yb_2Si_2O_7$, β-$Lu_2Si_2O_7$, and β-$Sc_2Si_2O_7$, are currently prioritized for EBCs.

Tian et al. [214] investigated the thermal conductivity of β-$Y_2Si_2O_7$, γ-$Y_2Si_2O_7$, β-$Yb_2Si_2O_7$, and β-$Lu_2Si_2O_7$ by a combination of first principles and experimental evaluation. The results showed that the four rare-earth

Table 2. Crystal types, spatial groups, and crystal systems of different rare-earth disilicates [213].

Crystal form	Element	Space group	Crystal system
A	La, Pr, Nd, Sm, Eu	$P4_122$-$P4_1$	Tetragonal
B (α)	Eu, Gd, Tb, Dy, Ho, Er	$P\bar{1}$-$P1$	Triclinic
C (β)	Ho, Er, Tm, Yb, Lu	$C2/m$-$C2$-Cm	Monoclinic
D (γ)	Er, Ho	$P2_1/a$	Monoclinic
E (δ)	Eu, Gd, Tb, Dy, Ho	P_{nam}-$P_{na}2_1$	Orthorhombic
F	Sm, Eu	$P\bar{1}$-$P1$	Triclinic
G	La, Ce, Pr, Nd, Sm	$P2_1/n$	Pseudo orthorhombic

disilicates had very low thermal conductivities, and the thermal conductivities showed significant anisotropy. Tian et al. [215] investigated the CMAS corrosion resistance of γ-$Y_2Si_2O_7$, β-$Yb_2Si_2O_7$, and β-$Lu_2Si_2O_7$ at 1300 °C and 1500 °C for 50 h. It was found that both β-$Yb_2Si_2O_7$ and β-$Lu_2Si_2O_7$ reacted violently with CMAS at 1300 °C. In contrast, the γ-$Y_2Si_2O_7$ had better resistance to CMAS corrosion at 1300 °C, but it would undergo phase transformation in high temperature and long-time corrosive environments, which was not suitable for the application of high stability EBCs. Combined with the optimization of Re_2SiO_5 performance by the high-entropy design, the rational high-entropy design is expected to provide a broader design space for the composition screening and performance modulation of $Re_2Si_2O_7$ materials for EBCs, and to promote their application in the next-generation EBCs.

Hao et al. [216] designed high-performance high-entropy $Re_2Si_2O_7$ materials by density functional theory with combinatorial chemistry methodology. The CTE was determined by phonon calculations at different volumes within the quasi-harmonic approximation, and the doped solid solution was found to exhibit lower thermal conductivity and a superior CTE by considering the three phonon processes by the Dybel-Gallaway model. Based on this theory, they designed two types of high-entropy ceramics, $(Er_{1/4}Eu_{1/4}Y_{3/4}Yb_{3/4})Si_2O_7$ and $(Er_{1/2}Lu_{1/2}Y_{1/2}Y_{b1/2})Si_2O_7$. The two ceramics exhibited a very low thermal conductivity (<0.23 $W \cdot m^{-1} \cdot K^{-1}$) at 1500 K and a coefficient of thermal expansion (5.1-5.2×10^{-6} K^{-1}) compatible with SiC. Guo et al. [217] prepared high-entropy $(Lu_{0.2}Yb_{0.2}Er_{0.2}Tm_{0.2}Sc_{0.2})_2Si_2O_7$ ($5Re_2Si_2O_7$) ceramics by solid-state sintering and characterized their thermal properties. There was no obvious absorption/exothermic peak in the DSC curve from room temperature to 1400 °C, which proved that this ceramic had good phase stability. The CTE is shown in Fig. 24. The $5Re_2Si_2O_7$ performed a lower CTE about 2.08-4.03×10^{-6} K^{-1}, which was close to that of SiC.

Sun et al. [218] investigated the high-temperature stability of γ-type $(Gd_{1/6}Tb_{1/6}Dy_{1/6}Tm_{1/6}Yb_{1/6}Lu_{1/6})_2Si_2O_7$ ($6Re_2Si_2O_7$) by thermogravimetry/differential thermal analysis (TG-DTA). The results are shown in Fig. 25(a), the $6Re_2Si_2O_7$ exhibited excellent thermal and crystal structure stability from room temperature to 1600 °C. The samples were heat-treated at 1800 °C and 1900 °C for 2 h, and then the cooled samples were analyzed by XRD, as shown in Fig. 25(b). The XRD peaks of the heat-treated samples all corresponded to the γ-type, and no diffraction peaks of other phases or polymorphs were detected, which indicated that $6Re_2Si_2O_7$ still had excellent crystal structure stability at 1800 °C and

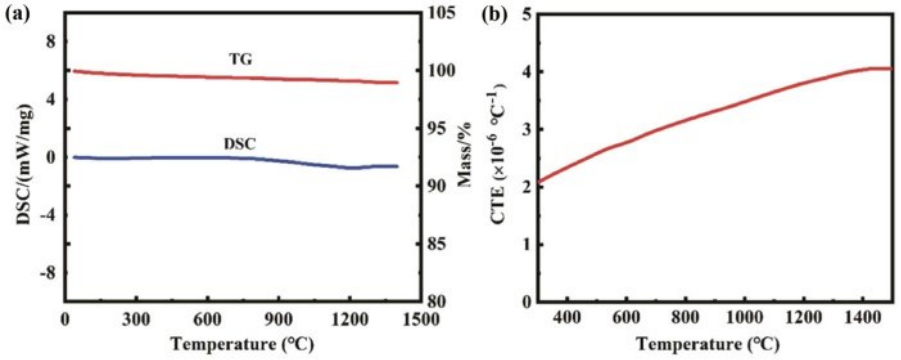

Fig. 24. (a) TG/DTA plots of $5Re_2Si_2O_7$ from room temperature to 1400 °C, (b) CTE curve of $5Re_2Si_2O_7$ from 300 °C to 1500 °C [217].

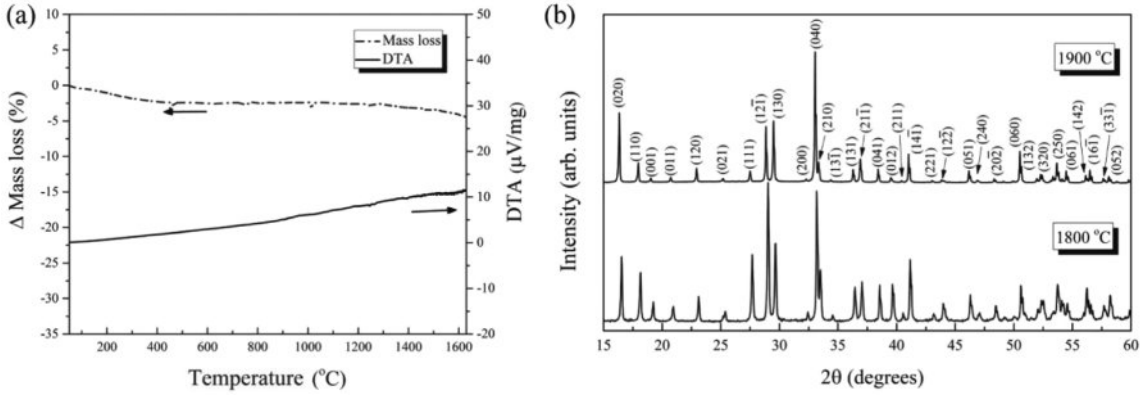

Fig. 25. (a) TG/DTA plots of $(Gd_{1/6}Tb_{1/6}Dy_{1/6}Tm_{1/6}Yb_{1/6}Lu_{1/6})_2Si_2O_7$ and (b) XRD patterns of specimens after calcined at 1800 and 1900 °C for 2 h [218].

1900 °C.

Currently, most of the researches on rare-earth silicate EBCs only improve the protective properties from a single perspective. Therefore, there is a lack of a material with excellent comprehensive performance that can fulfill multiple demands for thermodynamic and thermochemical properties in the complex operating environment of engines. The development of multifunctional coupled rare-earth silicates will be an essential aspect of the EBCs. In addition, the real service environment of the engine is very complex, and the current evaluation methods on rare-earth silicates are relatively single, lacking a complete environmental performance evaluation system. Therefore, the establishment of an aero-engine environment simulation platform and the development of scientific simulation test methods is an important research direction of EBCs. In terms of material development, systematic research on multi-rare-earth element/high-entropy rare-earth silicate materials is carried out to clarify the intrinsic connection and synergistic mechanism between the compositional structure, thermodynamic properties, and typical service performance of rare-earth silicate materials. Ultimately, the principle of performance regulation of high-entropy rare-earth silicates is proposed, and the comprehensive performance regulation of multifunctional rare-earth silicate materials is established.

Summary and Outlook

To fulfill the constant requirement for higher operating temperatures in aero-engines, thermal barrier coatings need to exhibit lower thermal conductivity and longer service life. This study examined the properties of a variety of thermal barrier coating materials, with researchers improving the thermodynamic properties by doping modification of YSZ. However, the high-temperature phase transformation of YSZ was the biggest shortcoming limiting its application. To overcome the high-temperature phase transition of ceramic materials, ZrO_2-based ceramic materials, $A_2B_2O_7$-type ceramic materials, rare-earth phosphates, rare-earth hafnates, yttrium aluminum garnet, perovskite oxides, magnetoplumbite compounds, high-entropy ceramics, rare-earth tantalates, rare-earth niobates, and rare-earth silicates are considered as promising ceramic materials for thermal barrier coatings. However, the thermodynamic performance of these materials as well as the thermal insulation performance has a discrepancy with the YSZ, so the performance of the ceramic materials needs to be optimized by using compositional modification. At present, the research on new ceramic materials for thermal barrier coatings mainly focuses on the thermodynamic properties, corrosion resistance, and thermal insulation properties of ceramic materials doped with rare-earth elements. Therefore, more relevant studies are needed to reveal the impact mechanisms of doping element types, doping element contents, coating preparation methods, and other factors on coating properties. The future development directions of advanced ceramic materials for thermal barrier coatings include:

With the continuous development of computer technology, the first principle technology has revolutionized the development of new materials, promoted the development of ceramic materials, and reduced the research and development cycle and cost. Through first-principle calculations, the thermodynamic properties, thermal insulation properties, and corrosion resistance of the new thermal barrier coating ceramic materials can be accurately predicted, providing a sufficient theoretical basis for the development of new materials and the regulation of their properties. In addition, the first principle can be used to explore the optimization mechanism of different elements for thermal barrier coatings from an atomic point of view. Therefore, combining material genetic engineering with the development of ceramic materials for thermal barrier coatings, screening stable crystal structures, and calculating the elastic modulus, thermal conductivity, coefficient of thermal expansion, and corrosion resistance of the materials is an important development direction in the future.

In the process of developing ceramic materials for thermal barrier coatings, microstructural adjustment of ceramic powders and ceramic coatings using controllable raw material powders to reduce the stress-strain mismatch within the coatings is the main way to regulate the structure and properties of thermal barrier coatings. Electro-spraying associated with phase inversion technology, as an emerging ceramic powder preparation method, has been successfully applied to promising new ceramic materials such as rare-earth zirconates, rare-earth tantalates, and rare-earth doped YSZ high-entropy materials, and the thermal barrier coatings prepared using hierarchical pore-structured powders have demonstrated superior thermal cycle life as well as lower thermal conductivities in high-temperature environments. Therefore, combining new ceramic materials with advanced powder preparation methods is conducive to further improving the thermodynamic properties of thermal barrier coatings and solving the problem of microstructural differences between different ceramic materials in the coating preparation process.

The operating environments of thermal barrier coatings include high temperatures, molten salt corrosion, and airflow erosion. Currently, most of the research on the properties of ceramic materials is carried out in a single test environment, and multi-environment coupling puts higher demands on the properties of ceramic materials. Therefore, it is necessary to establish the performance evaluation standards of different ceramic materials in the coupling environment, build a coupling environment test platform, study the failure mechanism of ceramic materials, and establish a performance prediction model, to provide sufficient theoretical support for

the optimization of the performance of new ceramic materials.

Acknowledgement

This work is supported by the National Natural Science Foundation of China (51702145), Liaoning Provincial Department of Education Project Services Local Project (FWDF202003).

Declarations

Conflict of interest The authors declare that they have no known competing financial interests or personal relationships that could have appeared to influence the work reported in this paper.

References

1. V.G.K. Anand and K.M. Parammasivam, J. Therm. Anal. Calorim. 146[2] (2021) 545-580.
2. J.B. Song, L.S. Wang, H. Dong, and J.T. Yao, Ceram. Int. 49[1] (2023) 1-23.
3. J.H. Perepezko, Science 326[5956] (2009) 1068-1069.
4. N.P. Padture, Nat. Mater. 15[8] (2016) 804-809.
5. D.P. Zhou, D.E. Mack, E. Bakan, G. Mauer, D. Sebold, O. Guillon, and R. Vassen, J. Am. Ceram. Soc. 103[3] (2020) 2048-2061.
6. J.H. Liu, Z. Lu, Y.W. Zhou, J. Zhang, and G.L. Lyu, J. Ceram. Process. Res. 24[2] (2023) 285-307.
7. Z.G. Liu, J.H. Ouyang, and Y. Zhou, J. Alloys Compd. 472[1-2] (2009) 319-324.
8. Z.W. Cai, J.S. Jiang, W.Z. Wang, Y.Z. Liu, and Z.M. Cao, Ceram. Int. 45[11] (2019) 14366-14375.
9. L. Wang, C. Deng, K.Y. Ding, S.Q. Guo, Z.D. Li, and X.P. Lin, Ceram. Int. 47[13] (2021) 18385-18396.
10. S.H. Jung, S.H. Jeon, L.J. Hyun, Y.G. Jung, I.S. Kim, and B.G. Choi, J. Korean Ceram. Soc. 53[6] (2016) 689-699.
11. D.H. Lee, B. Jang, C. Kim, and K.S. Lee, J. Ceram. Process. Res. 20[5] (2019) 499-504.
12. S.H. Kim, Z. Fu, K. Niihara, and S.W. Lee, J. Ceram. Process. Res. 12[2] (2011) 126-131.
13. B. Gleeson, J. Propul. Power 22[2] (2006) 375-383.
14. P.C. Tsai, J.H. Lee, and C.S. Hsu, Surf. Coat. Technol. 201[9-11] (2007) 5143-5147.
15. D.R. Clarke, and C.G. Levi, Annu. Rev. Mater. Res. 33 (2003) 383-417.
16. D.R. Clarke and S.R. Phillpot, Mater. Today 8[6] (2005) 22-29.
17. X.M. Song, Y. Ding, J.M. Zhang, C.F. Jiang, Z.W. Liu, C.C. Lin, W. Zheng, and Y. Zeng, J. Mater. Res. Technol. 23 (2023) 648-655.
18. Y. Han and J.F. Zhu, Top. Catal. 56[15-17] (2013) 1525-1541.
19. X.X. Zhu, G.L. Hou, J.K. Ma, X.Y. Zhang, Y.L. An, H.D. Zhou, J.M. Chen, and W.S. Li, Ceram. Int. 50[9] (2024) 14718-14730.
20. S.A. Tsipas, I.O. Golosnoy, R. Damani, and T.W. Clyne, J. Therm. Spray Technol. 13[3] (2004) 370-376.
21. G. Lyu, I.S. Kim, D. Song, H.M. Park, J.S. Kim, T. Song, S. Myoung, Y.G. Jung, and J. Zhang, Ceram. Int. 46[2] (2020) 1307-1313.
22. H. Jeon, I. Lee, and Y. Oh, Ceram. Int. 48[6] (2022) 8177-8185.
23. J.S. Wang, L.Y. Chen, M.D. Chen, Y.Y. Wu, Y.H. Wang, Y.S. Yu, J.B. Sun, B. Liu, and Q.S. Jing, Ceram. Int. 47[16] (2021) 22965-22975.
24. W. Fan, Y. Bai, Y.F. Wang, T. He, Y. Cao, Y. Zhang, X.B. Zhong, B.M. Li, Z.D. Chang, and Y.S. Ma, J. Alloys Compd. 829 (2020) 154525.
25. H.F. Liu, S.L. Liu, Q.L. Li, and Y.M. Li, Mater. Des. 31[6] (2010) 2972-2977.
26. P.C. Wang, Y.C. Zhao, M. Liu, H.P. Wang, G.Z. Ma, and H.D. Wang, Mater. Rep. 35[9] (2021) 9069-9076.
27. Y.X. Wang and C.G. Zhou, Ceram. Int. 42[11] (2016) 13047-13052.
28. L. Jin, C.Z. Jiang, H.Y. Xu, B. Zhang, C.G. Zhou, and H. Peng, Int. J. Lightweight Mater. Manuf. 2[3] (2019) 261-266.
29. H.T. Chen and J.G. Chang, J. Chem. Phys. 132 (2010) 214702.
30. X.D. Wei, G.L. Hou, D. Zhao, Y.L. An, and H.D. Zhou, Surf. Technol. 46[6] (2020) 92-103.
31. C. Mercer, J.R. Williams, D.R. Clarke, and A.G. Evans, Proc. R. Soc. A 463[2081] (2007) 1393-1408.
32. F. Yang, X.F. Zhao, and P. Xiao, Acta Mater. 60[3] (2012) 914-922.
33. M. Zhao, X.R. Ren, and W. Pan, J. Am. Ceram. Soc. 98[1] (2015) 229-235.
34. Y. Lyu, X. Shao, W.X. Wang, and H. Tang, J. Nanoelectron. Optoelectron. 14[11] (2019) 1597-1605.
35. L. Jin, Q.H. Yu, L.Y. Ni, and C.G. Zhou, J. Therm. Spray Technol. 21[5] (2012) 928-934.
36. G. Venkadesan, and J. Muthusamy, Ceram. Int. 45[3] (2019) 3166-3176.
37. M. Zhao, S.H. Zhang, and W. Pan, Rare Met. Mater. Eng. 44 (2015) 222-225.
38. D. Song, T. Song, U. Paik, G. Lyu, J. Kim, S. Yang, and Y.G. Jung, Surf. Coat. Technol. 400 (2020) 126197.
39. S.H. Jung, Z. Lu, Y.G. Jung, D. Song, U. Paik, B.G. Choi, I.S. Kim, X.Y. Guo, and J. Zhang, Surf. Coat. Technol. 323 (2017) 39-48.
40. L.L. Sun, H.B. Guo, H. Peng, S.K. Gong, and H.B. Xu, Ceram. Int. 39[3] (2013) 3447-1451.
41. Q.L. Li, W.H. Yang, and S.Q. Li, Therm. Spray Technol. 5[2] (2013) 26-30.
42. L. Guo, M.Z. Li, and F.X. Ye, Ceram. Int. 42[6] (2016) 7360-7365.
43. J. Tapia-López, M. Pech-Canul, and H.M. García, Front. Mater. 10 (2023) 1165245.
44. X.L. Zhang, Z.L. Lü, and Z.H. Jin, Rare Met. Mater. Eng. 34[8] (2005) 1267-1270.
45. Z.Q. Guo, L.Q. Zhang, Y. Qiao, Q. Gao, and Z.P. Xiao, Scr. Mater. 218 (2022) 114798.
46. Y.Q. Liu, G. Shao, and P. Tsakiropoulos, Intermetallics 9[2] (2001) 125-136.
47. B. Yu, Z. Li, K.X. Zhou, H.L. Tian, Y.C. Fang, X.M. Zhang, and G. Jin, J. Chin. Soc. Corros. Prot. 43[4] (2023) 812-820.
48. J. Kulczyk-Malecka, X. Zhang, J. Carr, F. Nozahic, C. Estournès, D. Monceau, A.L. Carabat, W.G. Sloof, S. Van der Zwaag, P.J. Withers, and P. Xiao, J. Eur. Ceram. Soc. 38[12] (2018) 4268-4275.
49. W.F. Kang, J.H. Chen, Y. Zhang, Q.Y. Zhang, T.X. Chen, and Y.Z. Gou, J. Mater. Res. Technol. 23 (2023) 1559-1569.
50. Y.H. Chen, R.L. Zhang, G.S. Zhang, P.Y. Jiang, J. Song, and X.W. Chu, Int. J. Thermophys. 42[5] (2021) 69.

51. C. Wang, X.F. Cui, G. Jin, Z.H. Gao, J.N. Jin, Z.B. Cai, and Y.C. Fang, Adv. Eng. Mater. 19[8] (2017) 1700149.
52. H. Zhang, J.Y. Yuan, W.J. Song, X. Zhou, S.J. Dong, S.W. Duo, J.S. Wang, X. Yang, J.N. Jiang, L.H. Deng, J.Q. Huang, and X.Q. Cao, Ceram. Int. 46[5] (2020) 6641-6651.
53. Y.C. Fang, X.F. Cui, G. Jin, B.W. Lu, F.Y. Wang, M. Liu, and X. Wen, Ceram. Int. 44[15] (2018) 18285-18293.
54. R.B. Ma, X.D. Cheng, and W.P. Ye, Appl. Surf. Sci. 357 (2015) 407-412.
55. T.T. Cheng, Z.P. Wang, S.J. Dai, S.C. Wang, and S.J. Xing, Ceram. Int. 48[5] (2022) 6443-6452.
56. F. Fu-k'ang, A.K. Kuznetsov, and É.K. Keler, Russ. Chem. Bull. 13 (1964) 1070-1075.
57. C.G. Liu, Y.H. Li, Y.D. Li, L.Y. Dong, J. Wen, D.Y. Yang, Q.L. Wei, and P. Yang, J. Nucl. Mater. 500 (2018) 72-80.
58. L.L. Cai, W. Ma, B.L. Ma, F. Guo, W.D. Chen, H.Y. Dong, and Y.C. Shuang, J. Therm. Spray Technol. 26[6] (2017) 1076-1083.
59. M. Uno, A. Kosuga, M. Okui, K. Horisaka, H. Muta, K. Kurosaki, and S. Yamanaka, J. Alloys Compd. 420[1-2] (2006) 291-297.
60. M. Saif, M. Shebi, A. Mbarek, A.I. Nabeel, R. Maalej, and R. Shokry, J. Photochem. Photobiol. A 301 (2015) 1-5.
61. L.Q. An, A. Ito, and T. Goto, Ceram. Int. 38[6] (2012) 4973-4977.
62. Z.J. Wang, G.H. Zhou, D.Y. Jiang, and S.W. Wang, J. Adv. Ceram. 7[4] (2018) 289-306.
63. J.W. Che, X.Z. Wang, X.Y. Liu, G.Y. Liang, and S.L. Zhang, Int. J. Heat Mass Transfer 182 (2022) 122038.
64. A. Chaudhry, A. Canning, R. Boutchko, M.J. Weber, N. Gronbech-Jensen, and S.E. Derenzo, J. Appl. Phys. 109[8] (2011) 083708.
65. A.Y. Zhang, M.K. Lü, Z.S. Zhang, G.J. Zhou, and Y.Y. Zhou, Solid State Sci. 10[1] (2008) 74-81.
66. E. Bakan and R. Vassen, J. Therm. Spray Technol. 26[6] (2017) 992-1010.
67. L. Zhou, F. Li, J.X. Liu, S.K. Sun, Y.C. Liang, and G.J. Zhang, J. Hazard. Mater. 415 (2021) 125596.
68. K. Bobzin, N. Bagcivan, T. Brögelmann, and B. Yildirim, Surf. Coat. Technol. 237 (2013) 56-64.
69. Q. Xu, J.D. Wang, L.H. Qi, H.Z. Miao, K. Mori, and T. Torigoe, Mater. Lett. 59[22] (2005) 2804-2807.
70. J. Wu, X.Z. Wei, N.P. Padture, P.G. Klemens, M. Gell, E. Garcí, P. Miranzo, and M.I. Osendi, J. Am. Ceram. Soc. 85[12] (2002) 3031-3035.
71. M. Stopyra, G. Moskal, M. Mikuskiewic, and O. Fabrichnaya, J. Eur. Ceram. Soc. 44[8] (2024) 5129-5137.
72. M.G. Gok and M. Karabas, Ceram. Int. 48[8] (2022) 11173-11180.
73. X.G. Liu, Z.Y. Shen, L.M. He, and R.D. Mu, Ceram. Int. 50[13] (2024) 22644-22652.
74. L. Guo, H.B. Guo, H. Peng, and S.K. Gong, J. Eur. Ceram. Soc. 34[5] (2014) 1255-1263.
75. G. Jin, Y.C. Fang, X.F. Cui, C. Wang, D. Zhang, X. Wen, and Q.B. Mi, Surf. Coat. Technol. 397 (2020) 125986.
76. H. Yamamura, H. Nishino, K. Kakinuma, and K. Nomura, J. Ceram. Soc. Jpn. 111[12] (2003) 902-906.
77. W. Ma, S.K. Gong, H.B. Xu, and X.Q. Cao, Surf. Coat. Technol. 200[16-17] (2006) 5113-5118.
78. X.Q. Cao, R. Vassen, W. Fischer, F. Tietz, W. Jungen, and D. Stöver, Adv. Mater. 15[17] (2003) 1438-1442.
79. X.F. Yu and Y.M. Liu, China Ceram. 48[4] (2012) 22-26.
80. H.S. Zhang, X.G. Chen, G. Li, X.L. Wang, and X.D. Dang, J. Eur. Ceram. Soc. 32[14] (2012) 3693-3700.
81. F.X. Shao, X.G. Chen, and H.S. Zhang, J. Ceram. 38[4] (2017) 559-563.
82. J.H. Liu, Z. Lu, Y.W. Zhou, S.G. Huang, H. Chen, and N. Xu, Surf. Technol. 51[7] (2022) 42-52.
83. W. Ma, H.B. Guo, S.K. Gong, and H.Y. Dong, J. Inorg. Mater. 24[5] (2009) 983-988.
84. R.S. Hay, P. Mogilevsky, and E. Boakye, Acta Mater. 61[18] (2013) 6933-6947.
85. Y.P. Fang, A.W. Xu, R.Q. Song, H.X. Zhang, L.P. You, J.C. Yu, and H.Q. Liu, J. Am. Chem. Soc. 125[51] (2003) 16025-16034.
86. T. Liu, B.Y. Ma, and W.Y. Zan, Refractories 57[2] (2023) 175-179.
87. S.S. Sujith, S.L.A. Kumar, R.V. Mangalaraja, A.P. Mohamed, and S. Ananthakumar, Ceram. Int. 40[9] (2014) 15121-15129.
88. C.L. Zhang, J.M. Fei, L. Guo, J.X. Yu, B.B. Zhang, Z. Yan, and F.X. Ye, Ceram. Int. 44[8] (2018) 8818-8826.
89. J. Yang, C.L. Wan, M. Zhao, M. Shahid, and W. Pan, J. Eur. Ceram. Soc. 36[15] (2016) 3809-3814.
90. M.Z. Li, Y.X. Cheng, L. Guo, Y.C. Zhang, C.L. Zhang, S.X. He, W. Sun, and F.X. Ye, J. Eur. Ceram. Soc. 37[10] (2017) 3425-3434.
91. C.R. Stanek, C. Jiang, B.P. Uberuaga, K.E. Sickafus, A.R. Cleave, and R.W. Grimes, Phys. Rev. B 80[17] (2009) 174101.
92. L.M. Lopato, V.P. Red'ko, G.I. Gerasimyuk, and A.V. Shevchenko, Powder Metall. Met. Ceram. 29 (1990) 318-320.
93. K.E. Sickafus, R.W. Grimes, J.A. Valdez, A. Cleave, M. Tang, M. Ishimaru, S.M. Corish, C.R. Stanek, and B.P. Uberuaga, Nat. Mater. 6[3] (2007) 217-223.
94. Z. Du, Q.S. Wang, Z. Ma, Y.K. Li, and Y.B. Liu, Rare Met. Mater. Eng. 40[S1] (2011) 268-270.
95. P. Yang, Y. L. An, D.Y. Yang, Y.H. Li, and J.M. Chen, Ceram. Int. 46[13] (2020) 21367-21377.
96. P.P. Liang, S.J. Dong, J.Y. Zeng, J.Y. Yuan, J.N. Jiang, L.H. Deng, X. Zhou, and X.Q. Cao, Ceram. Int. 45[17] (2019) 22432-22436.
97. M.C. Sun, Y.Q. Sui, K. Gao, C. Tan, L. Dai, G.P. Zhou, and Y.J. Zhang, Ceram. Int. 45[9] (2019) 212101-12105.
98. R.D. Shannon, Acta Crystallogr., Sect. A: Cryst. Phys., Diffr., Theor. Gen. Crystallogr. 32[5] (1976) 751-767.
99. A. Bogicevic and C. Wolverton, Phys. Rev. B 67[2] (2003) 024106.
100. A. Bogicevic, C. Wolverton, G.M. Crosbie, and E.B. Stechel, Phys. Rev. B 64[1] (2001) 014106.
101. P. Duan and C. Pascual, J. Mater. Sci. 19 (1984) 1178-1184.
102. D.L. Poerschke, J.S. Van Sluytman, K.B. Wong, and C.G. Levi, Acta Mater. 61[18] (2013) 6743-6755.
103. A.G. Karaulov and E.I. Zoz, Refract. Ind. Ceram. 40 (1999) 479-483.
104. S. Ueno, D.D. Jayaseelan, N. Kondo, T. Ohji, and S. Kanzaki, Ceram. Int. 30[6] (2004) 865-867.
105. K.Y. Lue, L.H. Dong, Y. Huang, G. Li, J.N. Jiang, S.J. Dong, and X.Q. Cao, Ceram. Int. 49[18] (2023) 30892-30896.
106. M. Poulos, S. Giaremis, J. Kioseoglou, J. Arvannitidis, D. Christofilos, S. Ves, M.P. Hehlen, N.L. Allan, C.E. Mohn, and K. Papagelis, J. Phys. Chem. Solids 162 (2022) 110512.
107. L.I. Kazakova, G.M. Kuz'micheva, and E.M. Suchkova, Inorg. Mater. 39[9] (2003) 959-970.
108. M.G. Shelyapina, V.S. Kasperovich, and P. Wolfers, J. Phys. Chem. Solids 67[4] (2006) 720-724.

109. P.J. Li, X. Bai, Y.Y. Liu, X.M. Wang, Y. Sun, and M.Y. Chu, J. Chin. Rare Earth Soc. 41[2] (2023) 214-231.
110. M. Gell, J.W. Wang, R. Kumar, J. Roth, C. Jiang, and E.H. Jordan, J. Therm. Spray Technol. 27[4] (2018) 543-555.
111. Y.J. Su, R.W. Trice, K.T. Faber, H. Wang, and W.D. Proter, Oxid. Met. 61[3-4] (2004) 253-271.
112. W.W. Shuai, H.J. Dou, Z.C. Duan, W. Qian, Z.B. Li, Y.Q. Hua, and J. Cai, Surf. Coat. Technol. 476 (2024) 130188.
113. Z.L. Xue, Y. Ma, and H.B. Guo, J. Eur. Ceram. Soc. 37[13] (2017) 4171-4177.
114. M.M. Gentleman and D.R. Clarke, Surf. Coat. Technol. 188 (2004) 93-100.
115. R.J.L. Steenbakker, J.P. Feist, R.G. Wellman, and J.R. Nicholls, J. Eng. Gas Turbines Power 131[4] (2009) 041301.
116. T. Kissel, J. Brübach, M. Euler, M. Frotscher, C. Litterscheid, B. Albert, and A. Dreizler, Mater. Chem. Phys. 140[2-3] (2013) 435-440.
117. M. Yu, G. Särner, C.C.M. Luijten, M. Richter, M. Aldén, R.S.G. Baert, and L.P.H. de Goey, Meas. Sci. Technol. 21[3] (2010) 037002.
118. M.D. Chambers and D.R. Clarke, Annu. Rev. Mater. Res. 39 (2009) 325-359.
119. L. He, B.B. Pu, W.S. Li, and W.M. Sun, Mater. Prot. 56[3] (2023) 13-19+48.
120. B. Liu, Y.C. Liu, C.H. Zhu, H.M. Xiang, H.F. Chen, L.C. Sun, Y.F. Gao, and Y.C. Zhou, J. Mater. Sci. Technol. 35[5] (2019) 833-851.
121. A.A. Bayode, S.S. Emmanuel, A. Osti, C.G. Olorunnisola, A.O. Egbedina, D.T. Koko, D.T. Adedipe, B. Helmreich, and M.O. Omorogie, J. Water Process Eng. 58 (2024) 104753.
122. X.H. Li, W. Ma, J. Wen, Y. Bai, L. Sun, B.D. Chen, H.Y. Dong, and Y.C. Shuang, J. Therm. Spray Technol. 26[3] (2017) 371-377.
123. C.J. Howard, K.S. Knight, B.J. Kennedy, and E.H. Kisi, J. Phys.: Condens.Matter 12[45] (2000) L677-L683.
124. D. Ligny and P. Richet, Phys. Rev. B 53[6] (1996) 3013-3022.
125. Y.C. Liu, B. Liu, H.M. Xiang, Y.C. Zhou, H.Q. Nian, H.F. Chen, G. Yang, and Y.F. Gao, J. Am. Ceram. Soc. 101[8] (2018) 3527-3540.
126. Y.C. Liu, W. Zhang, B.H. Wang, L.C. Sun, F.Z. Li, Z.H. Xue, G.H. Zhou, B. Liu, and H.Q. Nian, Ceram. Int. 44[14] (2018) 16475-16482.
127. W. Ma, D.E. Mack, R. Vassen, and D. Stöver, J. Am. Ceram. Soc. 91[8] (2008) 2630-2635.
128. Y. Liu, Y. Bai, E.B. Li, Y.W. Qi, C.W. Liu, H.Y. Dong, R.L. Jia, and W. Ma, Mater. Chem. Phys. 247 (2020) 122904.
129. J.X. Zhang, Y. Bai, E.B. Li, H.Y. Dong, and W. Ma, Int. J. Appl. Ceram. Technol. 17[4] (2020) 1608-1618.
130. L. Yang, Y.C. Liu, W. Zhang, G.H. Zhou, D.Y. Jiang, H.F. Chen, G. Yang, H.Q. Nian, and B. Liu, J. Am. Ceram. Soc. 103[3] (2020) 1992-2000.
131. W. Zhang, J.L. Zhao, P.Y. Wang, Y.C. Liu, P. Song, D.Y. Jiang, W.X. Li, Y.C. Zhou, L. Yang, H.Q. Nian, and B. Liu, Ceram. Int. 46[11] (2020) 17416-17422.
132. P.Z. Li, M. Xie, M. Zhao, X.W. Song, and S.L. An, Chin. Rare Earths 31[1] (2010) 26-29.
133. R. Gadow and M. Lischka, Surf. Coat. Technol. 151 (2002) 392-399.
134. W. Li, X.J. Zhou, Q.G. Lei, and S. Wang, Ceram. Int. 47[3] (2021) 3209-3218.
135. X. Min, Z.H. Huang, M.H. Fang, Y.G. Liu, C. Tang, and X.W. Wu, Inorg. Chem. 53[12] (2014) 6060-6065.
136. J.M.P.J. Verstegen, J.L. Sommerdijk, and J.G. Verriet, J. Lumin. 6[5] (1973) 425-431.
137. K.V. Yumashev, I.A. Denisov, N.N. Posnov, V.P. Mikhailov, R. Moncorgé, D. Vivien, B. Ferrand, and Y. Guyot, J. Opt. Soc. Am. B 16[12] (1999) 2189-2194.
138. B. Jiang, M.H. Fang, Z.H. Huang, Y.G. Liu, P. Peng, and J. Zhang, Mater. Res. Bull. 45[10] (2010) 1506-1508.
139. J.B. Sun, J.S. Wang, X. Zhou, S.J. Dong, L.H. Deng, J.N. Jiang, and X.Q. Cao, Ceram. Int. 44[5] (2018) 5572-5580.
140. J.B. Sun, Y. Hui, J.N. Jiang, L.H. Deng, and X.Q. Cao, Appl. Surf. Sci. 504 (2020) 144509.
141. J.J. Cui, J.H. Ouyang, and Z.G. Liu, J. Alloys Compd. 685 (2016) 316-321.
142. S. Tsukada, S. Kuroda, M. Nishijima, H. Araki, A. Yumoto, and M. Watanabe, Surf. Coat. Technol. 363 (2019) 95-105.
143. X.L. Chen, Y. Zhao, X.Z. Fan, Y.J. Liu, B.L. Zou, Y. Wang, H.M. Ma, and X.Q. Cao, Surf. Coat. Technol. 205[10] (2011) 3293-3300.
144. X.L. Chen, L.J. Gu, B.L. Zou, Y. Wang, and X.Q. Cao, Surf. Coat. Technol. 206[8-9] (2012) 2265-2274.
145. B.L. Zuo, Z.S. Khan, X.Z. Fan, W.Z. Huang, L.J. Guo, Y. Wang, J.Y. Xu, S.Y. Tao, K.Y. Yang, H.M. Ma, and X.Q. Cao, Surf. Coat. Technol. 219 (2013) 101-108.
146. B.L. Zuo, Z.S. Khan, L.J. Gu, X.Z. Fan, W.Z. Huang, Y. Wang, Y. Zhao, C.J. Wang, K.Y. Yang, H.M. Ma, and X.Q. Cao, Corros. Sci. 62 (2012) 192-200.
147. X.R. Lu, J.Y. Yuan, M.Y. Xu, Q. Hu, J.Q. Huang, L.H. Deng, J.N. Jiang, S.J. Dong, L. Liu, L. Qin, and X.Q. Cao, Ceram. Int. 47[20] (2021) 28892-28903.
148. Y.H. Wang, J.H. Ouyang, and Z.G. Liu, Mater. Des. 31[7] (2010) 3353-3357.
149. H.M. Xiang, Y. Xing, F.Z. Dai, H.J. Wang, L. Su, L. Miao, G.J. Zhang, Y.G. Wang, X.W. Qi, L. Yao, H.L. Wang, B. Zhao, J.Q. Li, and Y.C. Zhou, J. Adv. Ceram. 10[3] (2021) 385-441.
150. J.W. Yeh, S.K. Chen, S.J. Lin, J.Y. Gan, T.S. Chin, T.T. Shun, C.H. Tasu, and S.Y. Chang, Adv. Eng. Mater. 6[5] (2004) 299-303.
151. C.M. Rost, E. Sachet, T. Borman, A. Moballegh, E.C. Dickey, D. Hou, J.L. Jones, S. Curtarolo, and J.P. Maria, Nat. Commun. 6 (2015) 8485.
152. S. Akrami, P. Edalati, M. Fuji, and K. Edalati, Mater. Sci. Eng., R 146 (2021) 100644.
153. L. Guo, B.W. Li, Y.X. Cheng, and L. Wang, J. Adv. Ceram. 11[3] (2022) 454-469.
154. X.R. Ren, C.L. Wan, M. Zhao, J. Yang, and W. Pan, J. Eur. Ceram. Soc. 35[11] (2015) 3145-3154.
155. Y. Li, C. Geng, L.L. Li, J.L. Wang, J. Xia, X.H. Su, and P. Zhao, Ceram. Int. 50[3] (2024) 5676-5684.
156. X.W. Luo, L.R. Luo, X.F. Zhao, H.Y. Cai, S.S. Duan, C.H. Xu, S. Huang, H.Y. Jin, and S. Hou, J. Eur. Ceram. Soc. 42[5] (2022) 2391-2399.
157. Z.F. Zhao, H.M. Xiang, F.Z. Dai, Z.J. Peng, and Y.C. Zhou, J. Mater. Sci. Technol. 35[11] (2019) 2647-2651.
158. D. Song, M. Ryu, J. Kwon, G. Lyu, J. Kim, H.B. Jeon, T. Song, U. Paik, B.I. Yang, Y.G. Jung, and Y.S. Oh, Ceram. Int. 47[23] (2021) 33544-33553.
159. Y.H. Zhang, M. Xie, Z.G. Wang, R.D. Mu, X.W. Song, Y.B. Yu, J.X. Bao, F. Zhou, and W. Pan, Ceram. Int. 48[7] (2022) 9602-9609.
160. X.Y. Ping, B. Meng, C. Li, W. Lin, Y.Q. Chen, C.C. Fang, H. Zhang, W.K. Liang, and Q. Zheng, J. Am. Ceram. Soc. 105[7] (2022) 4910-4920.
161. L. Xu, H.J. Wang, L. Su, D. Lu, K. Peng, and H.F. Gao,

J. Eur. Ceram. Soc. 41[13] (2021) 6670-6676.
162. H.M. Zhang, Y. Song, W.W. Sang, Y.H. Guo, Y.K. Zhao, Y.Z. Zhao, S. Song, C.M. Li, R.T. Li, Z.Z. Li, H.S. Zhang, X.L. Zhang, and X.G. Chen, Ceram. Int. 48[6] (2022) 8380-8386.
163. H.S. Zhang, L.M. Zhao, W.W. Sang, X.G. Chen, A. Tang, and H.M. Zhang, Ceram. Int. 48[2] (2022) 1512-1521.
164. J. Feng, S. Shian, B. Xiao, and D.R. Clarke, Phys. Rev. B 90[9] (2014) 094102.
165. L. Chen, B.H. Li, and J. Feng, Prog. Mater. Sci. 144 (2024) 101265.
166. O.V. Voloshyna, I.A. Boiaryntseva, V.N. Baumer, A.I. Ivanov, M.V. Korjik, and O.T. Sidletskiy, Nucl. Instrum. Methods Phys. Res., Sect. A 764 (2014) 227-231.
167. Y. Yokogawa, M. Yoshimura, and S. Sōmiya, J. Mater. Sci. Lett. 9 (1990) 1181-1183.
168. S. Shian, P. Sarin, M. Gurak, M. Baram, W.M. Kriven, and D.R. Clarke, Acta Mater. 69 (2014) 196-202.
169. J. Wang, Q. Zheng, X.L. Shi, D.B. Li, Y. Yang, C. Li, and J. Feng, Surf. Coat. Technol. 456 (2023) 129222.
170. J. Wang, X.Y. Chong, R. Zhou, and J. Feng, Scr. Mater. 126 (2017) 24-28.
171. J. Wang, Y. Zhou, X.Y. Chong, R. Zhou, and J. Feng, Ceram. Int. 42[12] (2016) 13876-13881.
172. Y. Zhou, G.Y. Gan, Z.H. Ge, P. Song, and J. Feng, Mater. Today Commun. 26 (2021) 101927.
173. P. Wu, X.Y. Chong, and J. Feng, J. Am. Ceram. Soc. 101[5] (2018) 1823.
174. J. Wang, F.S. Wu, R.A. Zou, Y.S. Wu, M.D. Gan, J. Feng, and X.Y. Chong, J. Am. Ceram. Soc. 104[11] (2021) 5873-5882.
175. J.T. Zhu, Z.H. Lou, P. Zhang, J. Zhao, X.Y. Meng, J. Xu, and F. Gao, J. Inorg. Mater. 36[4] (2021) 411-417.
176. R. Abe, M. Higashi, Z.G. Zou, K. Sayama, Y. Abe, and H. Arakawa, J. Phys. Chem. B 108[3] (2004) 811-814.
177. M. Wakeshima, and Y. Hinatsu, J. Solid State Chem. 138[11] (2010) 2681-2688.
178. L. Chen, P. Wu, and J. Feng, Int. J. Appl. Ceram. Technol. 16[1] (2019) 230-242.
179. G.R. Li, H. Xie, G.J. Yang, G. Liu, C.X. Li, and C.J. Li, J. Am. Ceram. Soc. 100[9] (2017) 4240-4251.
180. L. Chen, and J. Feng, Adv. Ceram. 40[6] (2019) 367-397.
181. L. Chen, P. Song, and J. Feng, Scr. Mater. 152 (2018) 117-121.
182. W.W. Sang, H.S. Zhang, H.H. Chen, B. Wen, and X.C. Li, J. Inorg. Mater. 36[4] (2021) 405-410.
183. S. Ebisu, H. Morita, and S. Nagata, J. Phys. Chem. Solids 61[1] (2000) 45-65.
184. L. Chen, Y.H. Jiang, X.Y. Chong, and J. Feng, J. Am. Ceram. Soc. 101[3] (2018) 1266-1278.
185. L. Chen, B.H. Li, J. Guo, Y.K. Zhu, and J. Feng, J. Adv. Ceram. 11[4] (2022) 556-569.
186. H.W. Liu, L. Liu, H.M. Xiang, F.Z. Dai, X.H. Wang, M.Z. Huang, C.L. Wan, Y.B. Liu, H.Z. Li, and Y.C. Zhou, J. Eur. Ceram. Soc. 42[8] (2022) 3559-3569.
187. T.H. Yeh, W.C. Hsu, and C.C. Chou, J. Phys. IV 128 (2005) 213-219.
188. L. Chen, Y.T. Wang, M.Y. Hu, L.Y. Zhang, J.K. Wang, Z.B. Zhang, X.B. Liang, J. Guo, and J. Feng, Appl. Phys. Lett. 118[7] (2021) 071905.
189. A. Masuno, H. Inoue, K. Yoshimoto, and Y. Watanabe, Opt. Mater. Express 4[4] (2014) 710-718.
190. Z.Y. Wei, G.H. Meng, L. Chen, G.R. Li, M.J. Liu, W.X. Zhang, L.N. Zhao, Q. Zhang, X.D. Zhang, C.L. Wan, Z.X. Qu, L. Chen, J. Feng, L. Liu, H. Dong, Z.B. Bao, X.F. Zhao, L. Guo, L. Wang, B. Cheng, W.W. Zhang, P.Y. Xu, G.J. Yang, H.N. Cai, H. Cui, Y. Wang, F.X. Ye, Z. Ma, W. Pan, M. Liu, K.S. Zhou, and C.J. Li, J. Adv. Ceram. 11[7] (2022) 958-1068.
191. L. Chen, P. Wu, P. Song, and J. Feng, J. Am. Ceram. Soc. 101[10] (2018) 4503-4508.
192. J.T. Zhu, X.Y. Meng, J. Xu, P. Zhang, Z.H. Lou, M.J. Reece, and F. Gao, J. Eur. Ceram. Soc. 41[1] (2021) 1052-1057.
193. M.Z. Huang, X.Y. Liu, Y.J. Feng, C.L. Wan, W. Pan, J. Yang, and X.H. Zhao, J. Eur. Ceram. Soc. 41[1] (2021) 526-534.
194. N.P. Padture, npj Mater. Degrad. 3[1] (2019) 11.
195. M.B. Ruggles-Wrenn, and T.M. Williams, Int. J. Appl. Ceram. Technol. 17[5] (2020) 2074-2082.
196. Q.M. Liu, S.Z. Huang, and A.J. He, J. Mater. Eng. 17[5] (2020) 2074-2082.
197. S.K. Thimmappa, B.R. Golla, and V.V.B. Prasad, Silicon 14[18] (2022) 12049-12074.
198. E.J. Opila, J.L. Smialek, R.C. Robinson, D.S. Fox, and N.S. Jacobson, J. Am. Ceram. Soc. 82[7] (1999) 1826-1834.
199. J.L. Smialek, R.C. Robinson, E.J. Opila, D.S. Fox, and N.S. Jacobson, Adv. Compos. Mater. 8[1] (1999) 33-45.
200. D. Tejero-Martin, C. Bennett, and T. Hussain, J. Eur. Ceram. Soc. 41[3] (2021) 1747-1768.
201. Y. Xu, X.X. Hu, F.F. Xu, and K.W. Li, Ceram. Int. 43[8] (2017) 5847-5855.
202. Y.J. Jian, Y.F. Wang, R.J. Liu, F. Wan, and J. Zhang, Ceram. Int. 47[16] (2021) 22373-22381.
203. Z.L. Tian, J. Zhang, T.Y. Zhang, X.M. Ren, W.P. Hu, L.Y. Zheng, and J.Y. Wang, J. Eur. Ceram. Soc. 39[4] (2019) 1463-1476.
204. Z.L. Tian, L.Y. Zheng, J.M. Wang, P. Wan, J.L. Li, and J.Y. Wang, J. Eur. Ceram. Soc. 36[1] (2016) 189-202.
205. H.M. Xiang, Z.H. Feng, and Y.C. Zhou, J. Mater. Res. 29[15] (2014) 1609-1619.
206. Y.R. Li, Y.X. Luo, Z.L. Tian, J.M. Wang, and J.Y. Wang, J. Eur. Ceram. Soc. 38[10] (2018) 3539-3546.
207. K.N. Lee, D.S. Fox, and N.P. Bansal, J. Eur. Ceram. Soc. 25[10] (2005) 1705-1715.
208. X.M. Ren, Z.L. Tian, J. Zhang, and J.Y. Wang, Scr. Mater. 168 (2019) 47-50.
209. M. Ridley, J. Gaskins, P. Hopkins, and E. Opila, Acta Mater. 195 (2020) 698-707.
210. H. Chen, H.M. Xiang, F.Z. Dai, J.C. Liu, and Y.C. Zhou, J. Mater. Sci. Technol. 36 (2020) 134-139.
211. Z.L. Chen, Z.L. Tian, L.Y. Zheng, K.Y. Ming, X.M. Ren, J.Y. Wang, and B. Li, J. Adv. Ceram. 11[8] (2022) 1279-1293.
212. M.V. Ayyasamy, J.A. Deijkers, H.N.G. Wadley, and P.V. Balachandran, J. Am. Ceram. Soc. 103[8] (2020) 4489-4497.
213. B.Y. Zhou, Y.J. Cui, C.L. Wang, Z. Yue, J. Jiao, and B. Yu, J. Mater. Eng. 12 (2023) 12-23.
214. Z.L. Tian, L.Y. Zhang, Z.J. Li, J.L. Li, and J.Y. Wang, J. Eur. Ceram. Soc. 36[11] (2016) 2813-2823.
215. Z.L. Tian, X.M. Ren, Y.M. Lei, L.Y. Zheng, W.R. Geng, J. Zhang, and J.Y. Wang, J. Eur. Ceram. Soc. 39[14] (2019) 4245-4254.
216. S.Q. Hao, R.P. Oleksak, Ö.N. Dogan, and M.C. Gao, Acta Mater. 258 (2023) 119225.
217. X.T. Guo, Y.L. Zhang, T. Li, P.F. Zhang, K. Shuai, J. Li, and X.H. Shi, J. Eur. Ceram. Soc. 42[8] (2022) 3570-3578.
218. L.C. Sun, Y.X. Luo, X.M. Ren, Z.H. Gao, T.F. Du, Z. Wu, and J.Y. Wang, Mater. Res. Lett. 8[11] (2020) 424-430.